Master's Thesis

Enhancing the corrosion resistance of Mg–Sn–Al-based alloys by microalloying and surface modification

Daseul Lee

Department of Materials Science and Engineering

Graduate School of UNIST

2019

Enhancing the corrosion resistance of Mg–Sn–Al-based alloys by microalloying and surface modification

Daseul Lee

Department of Materials Science and Engineering

Graduate School of UNIST

Enhancing the corrosion resistance of Mg–Sn–Al-based alloys by microalloying and surface modification

A thesis
submitted to the Graduate School of UNIST
in partial fulfillment of the
requirements for the degree of
Master of Science

Daseul Lee

12. 17. 2018
Approved by

Advisor
Sung Soo Park

Enhancing the corrosion resistance of Mg–Sn–Al-based alloys by microalloying and surface modification

Daseul Lee

This certifies that the thesis of Daseul Lee is approved.

12. 17. 2018

Advisor: Sung Soo Park

Jung Gu Lee

Hu Young Jeong

Abstract

Through the Y microalloying and pulsed electron beam (PEB) treatment, the corrosion resistance of Mg–Sn–Al-based alloys has been greatly improved. The first method was microalloying of the Mg–8Sn–1Zn–1Al (wt.%) alloy with 0.04wt.% Y. The corrosion rates of Mg–8Sn–1Zn–1Al (wt.%) and Mg–8Sn–1Zn–1Al–0.04Y (wt.%) were measured in a 0.6 M NaCl solution and it showed that the average corrosion rate was reduced almost three times from 12.71 to 4.24 mmpy. Because of Y microalloying, the highly noble Al_5Fe_2 particle of TZA811 alloy has been changed to the core-shell particle of Al_8Fe_4Y and MgSnY, resulting into a decreased cathodic activity, ultimately increasing the corrosion resistance.

The second method was to selectively remove the Mg_2Sn precipitates on the surface of Mg–8Sn–1Zn–1Al–0.1Mn (wt.%), which is known as an Mg–Sn–Al-based alloy that has high corrosion resistance, to maintain high tensile strength while having better corrosion resistance. The average corrosion rates, measured with a 0.6 M NaCl solution, were 7.79 (as-extruded), 4.56 (PEB-treated), and 4.15 (T4-treated specimen) mmpy. Since the Mg_2Sn precipitates on the surface were removed, the cathodic activity was reduced, resulting in increased corrosion resistance. Also, the tensile strength was maintained because the Mg_2Sn precipitates were only removed on the surface to a depth of 10 μm.

Contents

List of Figures

List of Tables

I. Introduction

Mg is used for lightweighting because it is the lightest structural metal and its alloys have a high specific strength. Due to the recent fuel efficiency regulations in the automobile industry, interest towards the Mg and Mg alloys have increased. Among the commercial Mg alloys, Mg–Al-based alloys have high mechanical strength and corrosion resistance. If it has a high Al content, the flexibility of molten metal is high, so it is suitable for die-casting. However, the β-$Mg_{17}Al_{12}$ phase present in the Mg–Al-based alloys is not thermally stable, resulting in poor creep resistance [1]. This has led many people to turn their eyes toward Mg–Sn-based alloys, which have a similar mechanical strength of the Mg–Al-based alloys while showing excellent creep resistance. The excellent creep resistance of the Mg–Sn-based alloys is due to the presence of Mg_2Sn –which has a high fusion point within the microstructure of the alloys, and because of the excellent thermal stability of Mg_2Sn, the Mg–Sn-based alloys are reported to be defect-free even under a high extrusion speed of 25 m min^{-1} or more during hot extrusion [2-7]. For example, Kang et al. reported that Mg–Sn–Al–Si alloy, with thermally stable Mg_2Sn particles distributed at the matrix and grain boundary, has a higher tensile strength and creep resistance compared to the commercial AZ91 alloy [2].

There was a study on how to increase the mechanical properties of Mg–Sn-based alloys, and it reported that if you add Zn to the Mg–Sn-based alloy, it results in a finer and uniform distribution of Mg_2Sn precipitates [8,9]. Also, in the study of Sasaki et al., it was found that in the case of extruded Mg–Sn–Zn–Al alloy, Al caused a solid solution hardening and grain refinement, improving the mechanical property. This resulted in tensile yield strength of 308 MPa and compressive yield strength of 280 MPa, which is both higher than the current commercial Mg–Al–Zn and Mg–Zn-based alloys [10,11]. However, recent studies have shown that adding Al to the Mg–Sn-based alloy creates a highly noble Al_5Fe_2 phase that acts as a strong cathodic site, aggravating the corrosion resistance [12]. To compensate for this weakness, some studies attempted microalloying or changing extrusion conditions [13,14]. Ha et al. removed Al_5Fe_2 by microalloying Mn to the Mg–8Sn–1Al–1Zn alloy. Instead, it was reported that a core-shell shaped particle made out of AlFe (core) and Al_8Mn_5 (shell), which has a relatively low electrochemical potential, was created [13]. Baek et al. reported that by artificial cooling during the extrusion process, without changing alloy composition, the size and the volume fraction of the highly noble Al_5Fe_2 decreased, and the Mn content within the Al_5Fe_2 particle had increased, resulting in a decrease of the nobility of Al_5Fe_2 [14].

1.1 Y microalloying

However, the Mn used in the study of Ha et al. may have a detrimental effect on corrosion resistance due to its higher electrochemical potential compared to Mg. This study has looked for elements that could replace Mn and that have a low electrochemical potential.

Among the various alloying elements for Mg, Y is drawing interests from many since it increases the creep resistance [15,16], ignition resistance [17,18], and corrosion resistance [19-22]. Especially, it is noted that it improves corrosion resistance because the standard reduction potential of Y is -2.37 V, which is same as that of Mg. When Y forms an intermetallic compound with noble elements such as Fe or Mn, it decreases the nobility of the particles, resulting in a positive effect on corrosion resistance [21,22]. Baek et al. reported that alloying 0.25wt.% Y to the Mg–Al–Ca-based alloy decreases corrosion rate from 1.84 to 0.31 mmpy, and explained that it is because the Al_8Mn_5, which is the noblest intermetallic compound in the alloy, is changed to the less noble Al_8Mn_4Y or Al_2Y during the alloying process [21]. Mingo et al. presented in their research that alloying 0.5wt.% Y to Mg–9Al (wt.%) resulted in an 80% increase of corrosion resistance. This is because the Al–Fe intermetallic compound within the Mg–9Al has changed to Al–Y–Fe, which decreases the Volta potential difference between the Mg matrix and intermetallic compound. An analysis using the scanning Kelvin probe force microscopy (SKPFM) showed that the Volta potential had reduced more than 300 mV [22].

In this study, Y was selected as the alloying element, and it focused on the relationship between the corrosion properties and the microstructural changes of the extruded Mg–8Sn–1Zn–1Al alloy, caused by the Y microalloying.

1.2 PEB treatment

As mentioned earlier, it is reported that if Al is alloyed to the Mg–Sn-based alloy, a highly noble Al_5Fe_2 phase is created which aggravates corrosion resistance. However, it has been reported that not only highly noble particles influence the corrosion rate, but also the less noble Mg_2Sn precipitates has a negative effect on the corrosion resistance of Mg–Sn-based alloys. Ha et al. observed the microstructure of Mg–(2,4,6,8)Sn (wt.%) and measured the corrosion rates, showing that the corrosion rate proportionately increases as the volume fraction of Mg_2Sn increase. It has also reported that the Mg_2Sn precipitates become a pitting corrosion site [23]. However, removing Mg_2Sn precipitates to increase corrosion resistance will also result in reducing mechanical strength. For example, Cheng et al. showed that as the weight percent of Sn increases in the extruded Mg–(6-8wt.%)Sn alloy, the tensile and compressive strengths become stronger. At the same time, when the weight percent of Sn increases, the volume fraction of Mg_2Sn increases while the grain size remains almost the same, which shows that there is a close relationship between Mg_2Sn precipitates and mechanical strength [24].

PEB treatment, which is a method of surface finishing, can rapidly heat the temperature of the target material to 10^7 K s^{-1} and has a fast cooling speed so that it can cause phase transformation at the surface of metal [25]. When PEB treatment was applied to the AZ91 Mg alloy, it melted to a depth of ~15 μm, and it improved the corrosion resistance due to the increase of melting of $Mg_{17}Al_{12}$ intermetallic compound and an increase of Al content within the melted layer [26-29].

In this study, PEB treatment was applied on the Mg–8Sn–1Zn–1Al–0.1Mn (wt.%) alloy, which is a type of Mg–Sn-based alloy that has high corrosion resistance. The microstructure, corrosion, and tensile properties of the PEB-treated specimen were compared with those of the as-extruded and T4-treated specimens of the same alloy.

II. Theoretical review

2.1 Corrosion of Mg

Cathodic partial reaction: $2\ H^+ + 2\ e^- \rightarrow H_2$

Anodic partial reaction: $2\ Mg \rightarrow 2\ Mg^{2+} + 2\ OH^- + H_2$

Chemical reaction: $2\ Mg^+ + 2\ H_2O \rightarrow 2\ Mg^{2+} + 2\ OH^- + 2\ H_2$

Overall reaction: $2\ Mg + 2\ H^+ + 2\ H_2O \rightarrow 2\ Mg^{2+} + 2\ OH^- + 2\ H_2$

2.2 Corrosion factors of Mg and Mg alloys

2.2.1. Nobility of Mg

As you can see in Table 1, Mg has relatively low E°. It means that Mg is basically active metal. For instance, E° of the Mg is -2.37 V while E° of the Fe and Al is -0.44 and -1.68 V, respectively.

Table 1. E° of various kinds of metal.

Element	Reaction	E° (V)
Au	$Au^+ + e^- \rightarrow Au$	1.69
Au	$Au^{3+} + 3e^- \rightarrow Au$	1.50
Ag	$Ag^+ + e^- \rightarrow Ag$	0.80
Cu	$Cu^+ + e^- \rightarrow Cu$	0.52
Cu	$Cu^{2+} + 2e^- \rightarrow Cu$	0.34
Fe	$Fe^{2+} + 2e^- \rightarrow Fe$	-0.44
Mn	$Mn^{2+} + 2e^- \rightarrow Mn$	-1.18
Ti	$Ti^{2+} + 2e^- \rightarrow Ti$	-1.60
Al	$Al^{3+} + 3e^- \rightarrow Al$	-1.68
Mg	$Mg^{2+} + 2e^- \rightarrow Mg$	-2.37
Y	$Y^{3+} + 3e^- \rightarrow Y$	-2.37
Li	$Li^+ + e^- \rightarrow Li$	-3.04

2.2.2. Galvanic corrosion

When certain metal contact with other types of metal, the difference in electrochemical potential results in a galvanic cell. Among the two metals, the metal with the nobler potential becomes the cathode and the one with the less noble potential becomes the anode. In the galvanic cell, corrosion of the cathode is prevented while the corrosion of the anode is accelerated. As explained in 2.2.1, the standard reduction potential of Mg is very low, so it is highly likely to become an anode when it contacts with other engineering metal [30]. This is called the macrogalvanic corrosion and Fig. 1 (a) shows the schematic diagram of this process.

Mg alloy does not have a uniform microstructure, so galvanic coupling occurs inside the alloy even when it does not contact with another metal. The galvanic corrosion occurs due to secondary-phase or impurity-containing intermetallic particle; sometimes it even occurs because of the difference in solid solution concentration [30]. This is called the microgalvanic corrosion and Fig. 1 (b) shows the schematic diagram of this process. Microgalvanic corrosion is observed very often within Mg and Mg alloys.

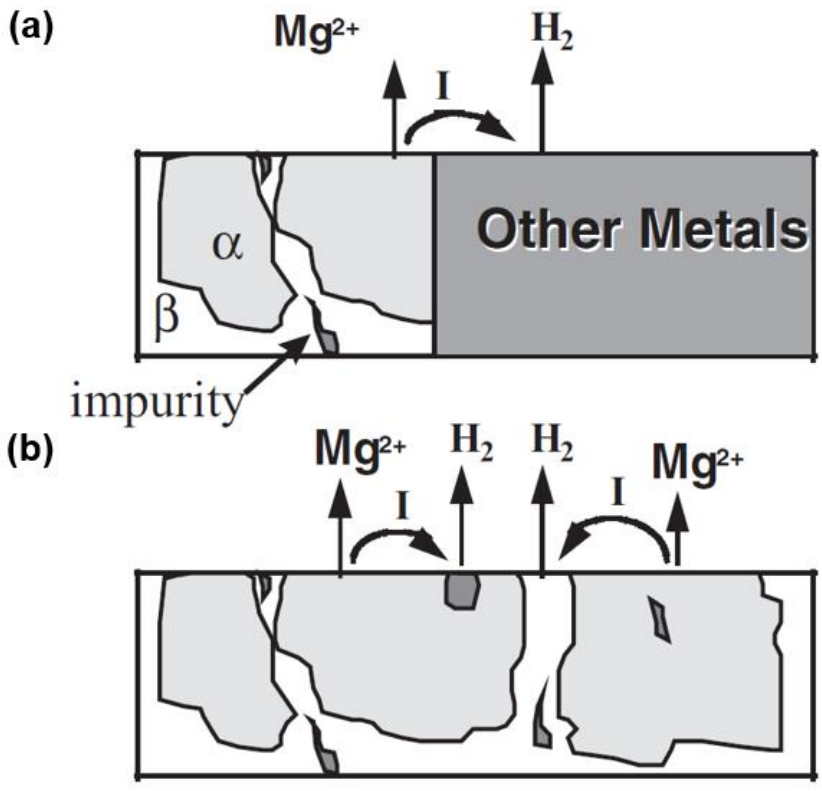

Fig. 1. Schematic diagram of (a) macrogalvanic and (b) microgalvanic corrosion [30].

2.2.3. Impurities

Hanawalt et al. found that elements such as Al, Sn, and Na in binary Mg alloy had almost no effect on the corrosion rate, even if they alloyed for more than 5wt.%. However, the four elements of Fe, Ni, Cu, and Co were found to increase the corrosion rate even when only 0.2wt.% was included [31]. Later, through the study of Hillis et al., it was reported that the corrosion rate of Mg could be increased 10 to 100 times more due to Fe, Ni, and Cu [32]. The study explained that this happens because these elements have a low solubility level in Mg while having a higher electrochemical potential compared to Mg, resulting in becoming a strong cathodic site [33]. Fig. 2 shows a diagram that depicts a 'Tolerance limit' of impurities where the corrosion rate increases rapidly as the amount of impurity increases in the Mg and Mg alloys. This is because if the impurity content exceeds the tolerance limit, the impurities will be segregated to become a cathodic site [34,35]. According to Hanawalt et al., the corrosion rate stays under 0.3 mmpy when the Fe amount is lower than 170 ppm, which is the tolerance limit of Fe. But the corrosion rate soars up to 3 ~ 200 mmpy when the Fe amount goes over 170 ppm [31,36].

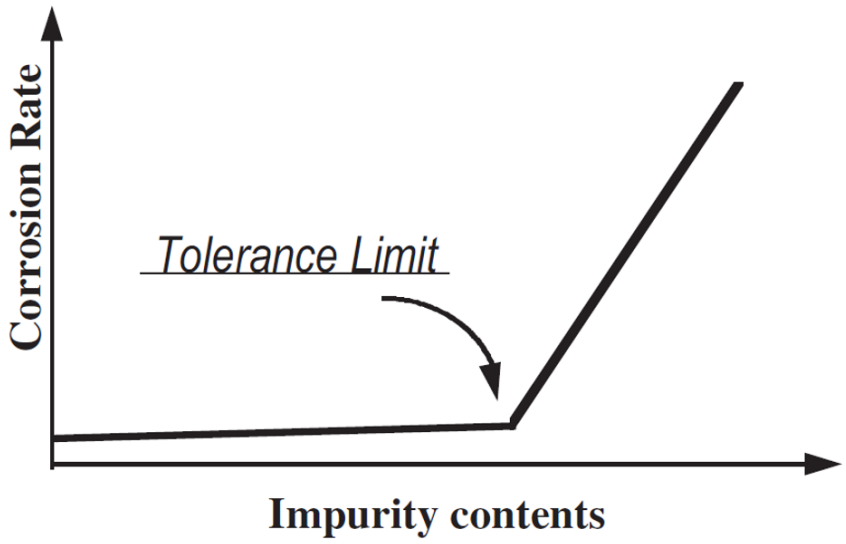

Fig. 2. Schematic diagram of tolerance limit of impurities [35].

However, an experiment of Yang et al. showed that the corrosion rate could be increased even when the impurity level is below the tolerance limit [37]. In the experiment, the corrosion rate of pure Mg

was measured to be 87 ~ 120 mmpy, even when the amount of Fe was 25 ppm, which is below the tolerance limit. Fig. 3 shows the results of experiments done by Hanawalt et al. and Yang et al. When analyzing the compositions of several pure Mg samples used in each experiment, the Si amount inside the pure Mg used by Hanawalt et al. was less than 10 ppm, whereas the Si contained in pure Mg used by Yang et al. was over 170 ppm. In the Mg–Fe binary phase diagram, it shows that Fe will segregate if the Fe is above 179 ppm. However, if you draw a Mg–Fe–Si ternary phase diagram where the Fe is at 25 ppm, it shows that when the Si is above 50 ppm, a Fe–Si intermetallic phase appears. Si plays an important role in creating a Fe rich particle [33,37]. As seen in these results, the elements of Fe, Ni, Cu, and Co in Mg have a fatal effect on the corrosion resistance of Mg and Mg alloys. Especially, if there is a sufficient amount of Si inside Mg, even the small amount of Fe will drastically decrease the corrosion resistance.

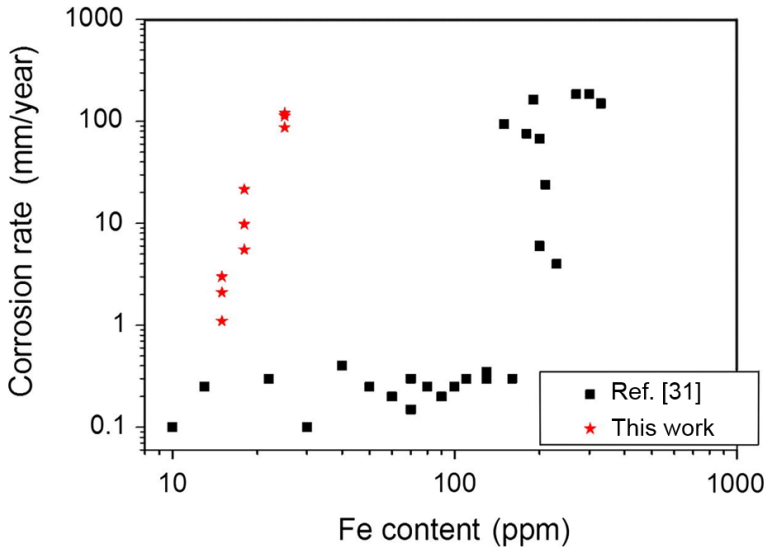

Fig. 3. Corrosion rates of several pure Mg samples which have different Fe and Si content [37].

2.2.4. Secondary-phase

Pure Mg is mainly used in an alloyed form because its mechanical strength is not high enough to be used as an engineering metal. The secondary-phase, which is produced by alloying, is in most cases, nobler than Mg matrix and causes microgalvanic corrosion. For example, the corrosion potentials (E_{corr}) of $Mg_{17}Al_{12}$, which is the secondary-phase of Mg–Al-based alloys, and Mg were -1.20 and -1.65 V_{SCE} respectively. The corrosion potential measurement was conducted after the immersion for 2 h in deaerated 5wt.% NaCl solution saturated with $Mg(OH)_2$ (pH 10.5) [38]. It was observed that the

secondary-phase in Mg–Al-based alloys such as AZ21, AZ501, and AZ91 and Mg matrix form the galvanic coupling [39,40].

2.3 Corrosion prevention of Mg and Mg alloys

2.3.1. Purifying

By using high purity Mg, you can prevent the corrosion occurring from impurities such as Fe, Ni, Cu, and Co. The purity of Mg can be improved by using the melting and boiling point of Mg. Fig. 4 shows the distillation device used in this process. First, apply heat over 900 °C to vaporize Mg. Then, the vaporized Mg will touch the relatively cold container of 700 °C and turn into a liquid state. If the liquefied Mg is solidified, you can obtain the Mg of an ultra-high purity. The final product will contain only 2 ppm of impurities [41]. The corrosion rates of high purity Mg (HP Mg) and ultra-high purity Mg (UHP Mg) were compared in the 3.5wt.% NaCl solution saturated with $Mg(OH)_2$. The results showed that the corrosion rates of the HP Mg (20 ppm Fe) were 0.38 and 0.67 mmpy, and the corrosion rate of the UHP Mg (1.6 ppm Fe) was 0.25 mmpy, proving that the Mg with higher purity is more resistant to corrosion [42].

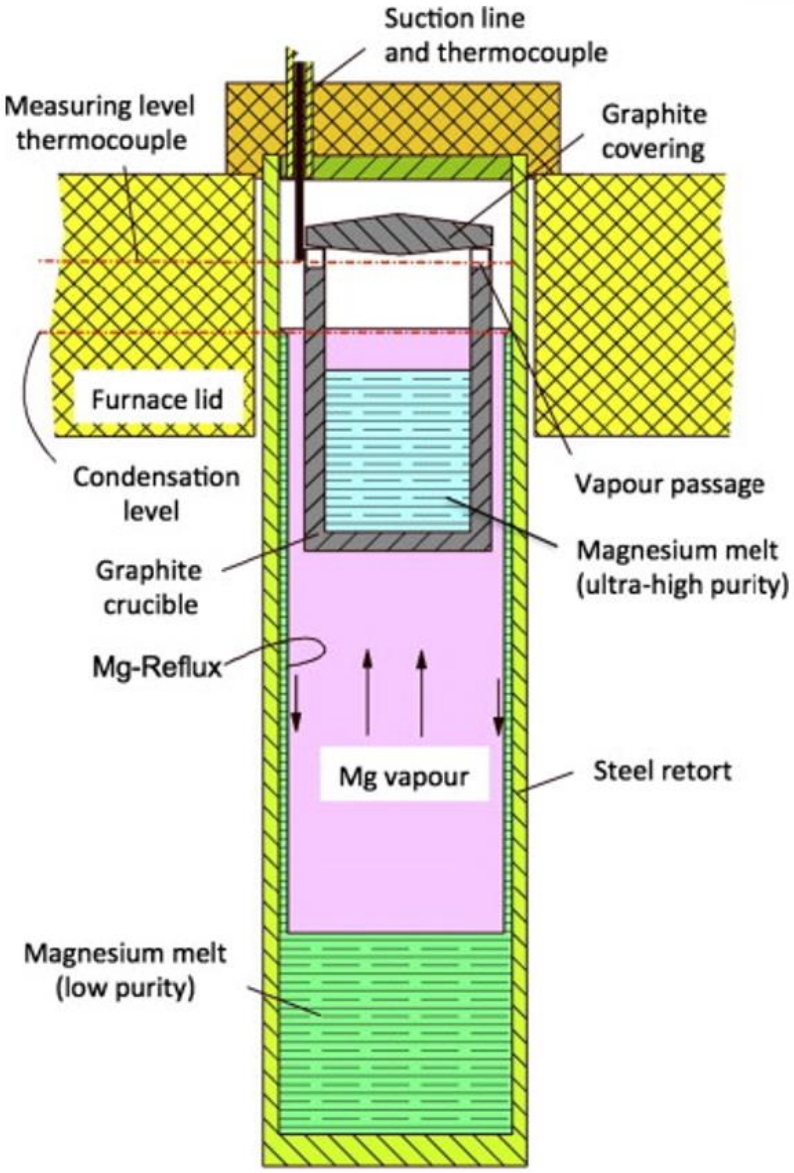

Fig. 4. Schematic illustration of Mg distillation device [41].

2.3.2. Compositional modification

There are many ways to improve corrosion resistance through alloying modification. The first way is to lower the electrochemical potential of the noble intermetallic phases. As shown in the phase diagram in Fig. 5, if a certain amount of Mn is added to the Mg–3Al (wt.%) alloy, the Fe particle in the form of $Al_{61}Fe_{31}$ disappears and Al–Fe–Mn and Al_8Mn_5 are created instead. The Fe rich intermetallic particle, which severely deteriorates the corrosion resistance of Mg, disappears by simply putting in Mn.

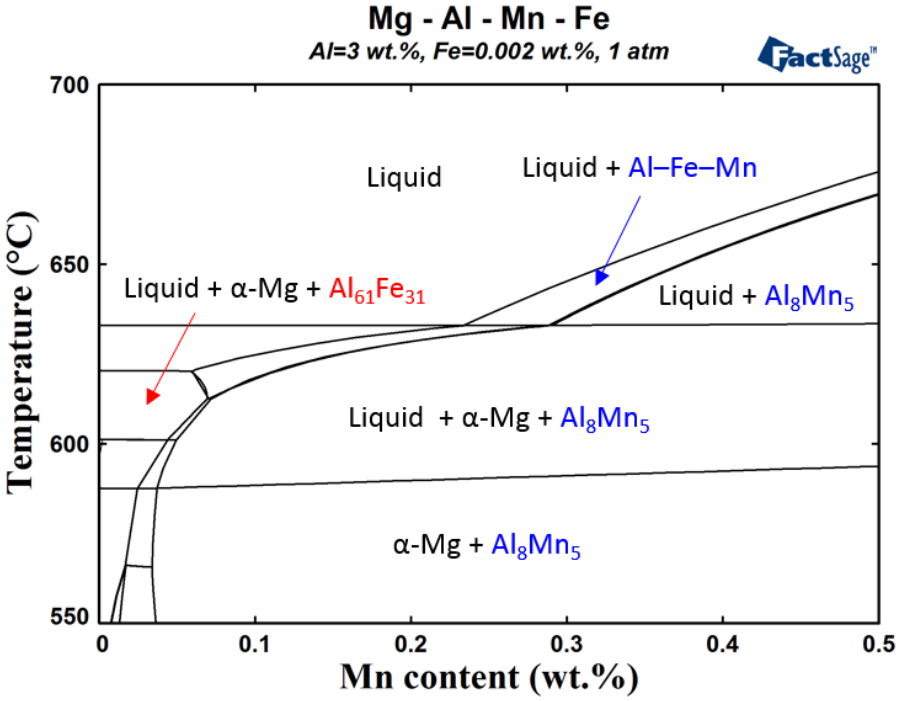

Fig. 5. Phase diagram of Mg–3Al–Mn (wt.%) alloy.

The second way is connecting the secondary-phase. $Mg_{17}Al_{12}$, the secondary-phase of Mg–Al-based alloys, usually acts as cathode and causes microgalvanic corrosion. However, when it is connected, it becomes a corrosion barrier as shown in Fig. 6. This happens because $Mg_{17}Al_{12}$ is nobler than α-Mg [30,38]. According to Kim et al., when a 0-2wt.% Ca is added to the Mg–5Al (wt.%) alloy, the grain size is reduced, resulting in a connection of β-$Mg_{17}Al_{12}$ phase. It is reported that as the amount of Ca increases, the polarization resistance (R_p) also increases, resulting in an improved corrosion resistance [43].

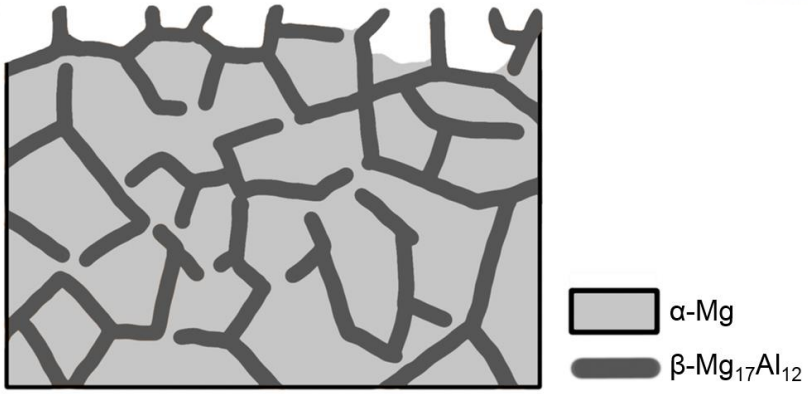

Fig. 6. Schematic illustration of barrier effect of secondary-phase.

2.3.3. Surface modification

The advantage of surface modification is that it can improve the corrosion resistance without damaging the original mechanical properties of Mg alloy. This is because when you use surface modification, most of the bulk alloy remains intact and only a small part of the bulk metal's properties changes. Types of surface modification include anodizing, surface conversion, laser surface melting, and PEB treatment.

2.4 Evaluation of corrosion

2.4.1. Immersion test [44]

The immersion test is the most common method of measuring the corrosion rate. First, immerse the specimen in a sufficient amount of solution more than 0.2 mL mm^{-2}. To measure the amount of reduced weight after the immersion, the oxide must be removed. In the case of Mg and Mg alloys, a chromic acid with a concentration of 180 g L^{-1} is used, and this process is called cleaning. After cleaning, the amount of mass loss is identified, and the corrosion rate is calculated using the formula below.

Corrosion rate = (K × W) / (A × T × D)

K = constant (8.76×10^4 for mmpy)

W = mas loss in g during cleaning

A = area in cm^2

T = time of exposure in hours

D = density in g cm^{-3}

2.4.2. H_2 evolution test

The H_2 evolution test is a method to determine the corrosion rate of Mg and Mg alloys; it utilizes the generation of a single hydrogen molecule when one Mg atom is dissolved during the corrosion reaction.

Corrosion in acidic solution: $Mg + 2\ H^+ \rightarrow Mg^{2+} + H_2$

Corrosion in neutral or basic solution: $Mg + 2\ H_2O \rightarrow Mg^{2+} + 2\ OH^- + H_2$

Theoretically, the amount of weight reduced can be calculated from the measured volume of H_2 evolution test by knowing the number of dissolved moles [45]. This method of experiment is advantageous since it has a small room for experimental error and it is easy to perform since you do not have to remove the oxide. Also, it is easy to monitor the whole corrosion process and corrosion rate

[30]. By setting it up in the form of Fig. 7, the volume of H_2 generated by the specimen can be easily measured by using the scale of the burette.

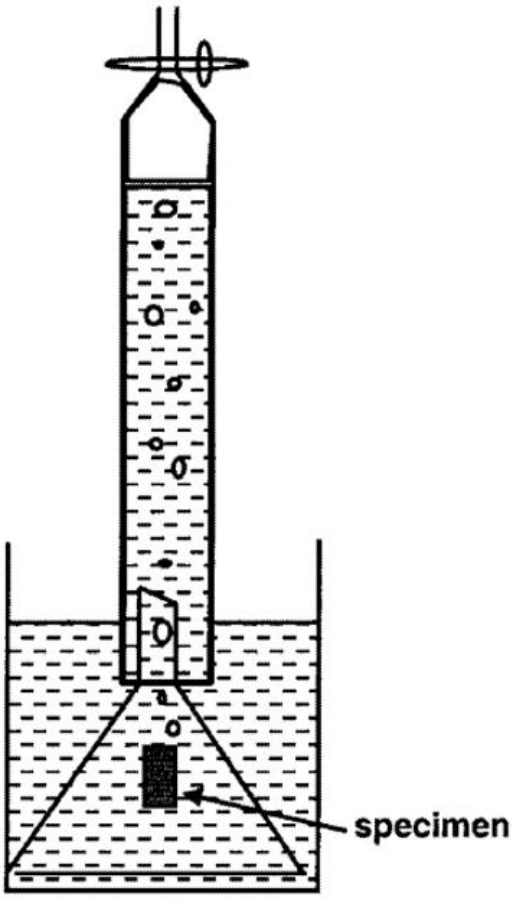

Fig. 7. Schematic illustration of hydrogen evolution test [45].

2.4.3. Potentiodynamic polarization test [46]

It takes several days to determine the corrosion resistance of the alloy by using the immersion test or the H_2 evolution test. However, the potentiodynamic polarization test can be used to determine the corrosion resistance of the alloy within a few hours.

Fig. 8 is a potentiodynamic polarization curve, which shows the change of electrode potential depending on the size of the current density. Under Faraday's law, the corrosion rate can be calculated by using the potentiodynamic polarization curve through the following formula.

$r = 0.00327 \frac{aicorr}{nD}$ (in mmpy)

r = corrosion rate

a = atomic weight

i_{corr} = corrosion current density

n = number of electrons exchanged per atom

D = density of metal

Here, i_{corr} is obtained through the Tafel extrapolation method. But in the case of Mg and Mg alloys, an accurate i_{corr} cannot be obtained by using the Tafel extrapolation method, so the potentiodynamic polarization curve is not used to calculate the corrosion rate of Mg and Mg alloys. Instead, the corrosion is analyzed by using the E_{corr}, cathodic current density ($i_{cathodic}$), and anodic current density (i_{anodic}), which are all obtainable through the potentiodynamic polarization curve.

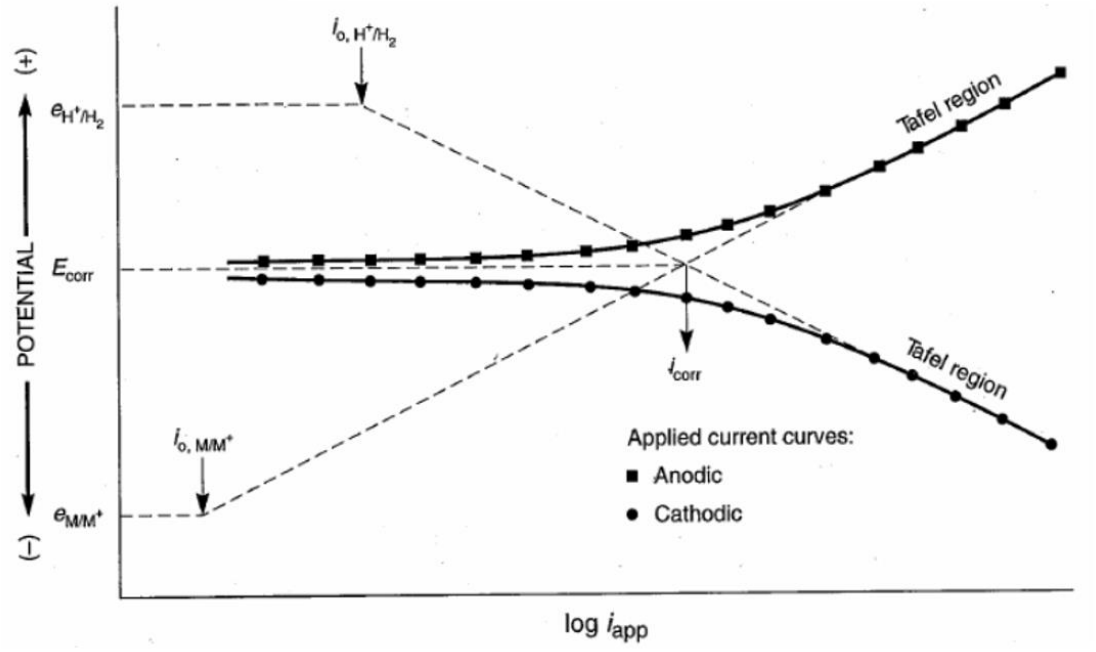

Fig. 8. Potentiodynamic polarization curve [46].

III. Influence of Y microalloying

3.1 Experimental

3.1.1. Specimen preparation

Table 2 shows the analyzed compositions (wt.%) of the Mg–8Sn–1Zn–1Al (TZA811) and Mg–8Sn–1Zn–1Al–0.04Y (TZAW8110) alloys used in this study. The billets were prepared by induction melting in the graphite crucible, under the inert atmosphere of CO_2 and SF_6. Then, the molten metals were poured into a steel mold that was preheated at 200 °C. Before extrusion, the diameter and height of the cast billets were 70 mm and 120 mm respectively. The cast billets were homogenized for 3 h at 500 °C and then water-quenched. Round solid profiles with a diameter of 11.8 mm were prepared by direct extrusion process under the initial billet temperature of 250 °C and the extrusion speed of 2.4 m min^{-1}.

Table 2. Analyzed compositions (wt.%) of the TZA811 and TZAW8110 alloys used in this study.

Alloy	Sn	Zn	Al	Y	Fe	Mn	Si	Mg
TZA811	7.34	0.89	0.92	<0.001	0.003	0.010	0.003	bal.
TZAW8110	7.66	0.78	0.78	0.042	0.003	0.015	0.002	bal.

3.1.2. Microstructure characterization

The middle part of the extruded material was used to observe the microstructure; the observation was done in a perpendicular direction to the extrusion direction (ED). Samples were prepared by grinding with SiC papers up to 1200 grit under the water atmosphere, and they were then polished using a 1 μm diamond paste and a 0.04 μm colloidal silica solution under an ethanol atmosphere. The microstructure was observed with the optical microscopy (OM) and the Quanta 200 scanning electron microscope (SEM) equipped with an energy dispersive spectrometer (EDS). It was also observed with a JEM-2100F Cs-corrected electron microscope (TEM) equipped with EDS.

3.1.3. Corrosion evaluation

The corrosion characteristics were evaluated through an immersion and H_2 evolution test at 25 °C, 0.6 M NaCl solution. In the case of the immersion test, after 72 h of immersion, the weight reduction was measured by removing the oxide using the 200 g L^{-1} CrO_3 solution. The H_2 evolution test was performed to measure the volume of generated H_2 gas as time passes. The H_2 evolution test was performed for 72 h.

In addition, the corrosion characteristics were evaluated by conducting a potentiodynamic polarization test at 25 °C, 0.6 M NaCl solution. The 0.6 M NaCl solution, which was used in the potentiodynamic polarization test, was deaerated by injecting N_2 gas. For the potentiodynamic polarization test, three-electrode cell -composed of a working electrode, saturated calomel reference electrode (SCE), and Pt plate counter electrode- were used. Potentiostat was used as the test equipment. The polarization test measured from -0.3 V_{SCE} versus E_{corr} to pitting potential (E_{pit}), based on the scan rate of 1 mV s^{-1}.

SKPFM was used to measure the relative Volta potential between the intermetallic particle and α-Mg matrix. The Pt-coated conducting tip was modulated by the AC modulation of 0.3 V at 70 kHz, which was generated by a lock-in amplifier. All SKPFM data was measured at 25 ℃ and a relative humidity of 40 ± 5%.

3.2 Results

3.2.1. Microstructure

Fig. 9 shows the SEM micrographs of TZA811 and TZAW8110 alloys observed in the perpendicular direction of the extruded direction to compare the changes in microstructure caused by 0.04wt.% Y microalloying. Fig 9 (a) is the extruded TZA811 alloy, which shows Mg_2Sn precipitates and highly noble Al_5Fe_2 particle that was previously reported [12]. Fig 9 (b), displaying the microstructure of the extruded TZAW8110 alloy, shows the same Mg_2Sn precipitates that were observed in TZA811, but the Al_5Fe_2 intermetallic phase was not found. Instead, particle A that was not observed in TZA811, was found in TZAW8110. In the SEM micrograph, particle A looked like a core-shell.

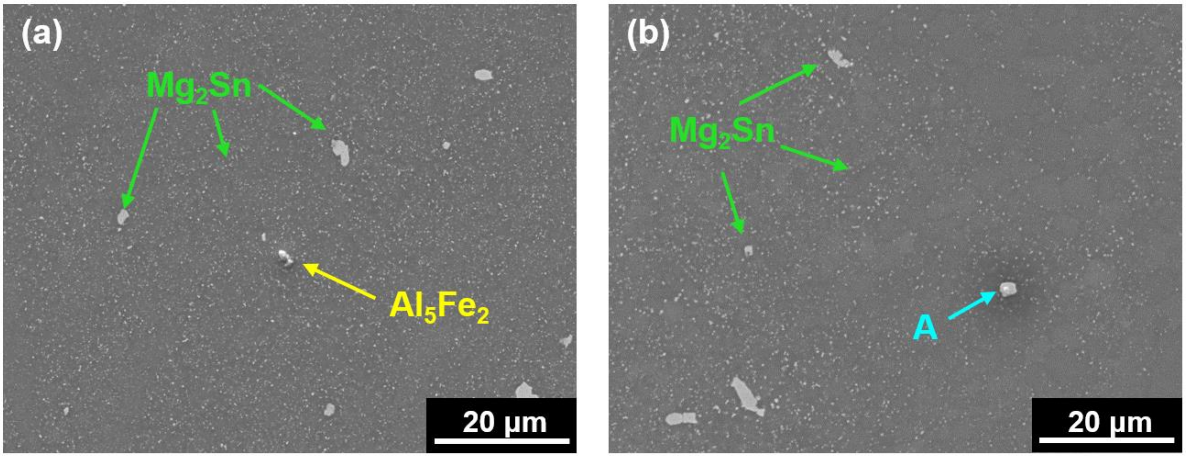

Fig. 9. SEM micrographs of the extruded (a) TZA811 and (b) TZAW8110 alloys.

EDS mapping was conducted to find out what particle A was made of. Fig. 10 (a) is the SEM micrograph of the particle A and Fig 10 (b-g) represent the corresponding EDS mapping images for each element. In Fig. 10, Al, Y, and Fe were detected at the center of the particle A and there were a lot of Sn and Y in the shell. Fig. 10 (h) and (i) show the diffraction patterns (DP) of the core and the shell, which were identified through TEM analysis. Fig. 10 (h) is the DP earned from the core. It shows a tetragonal structure and the lattice parameter was identical with Al_8Fe_4Y with a = 0.874 nm and c = 0.504 nm. Fig. 10 (i) is the DP earned from the shell. It shows the orthorhombic structure and the lattice parameter was identical with MgSnY with a = 0.697 nm, b = 1.033 nm, and c = 1.327 nm. All the Al_8Fe_4Y particles observed at the extruded TZAW8110 alloy were wrapped in MgSnY particles. Some core-shell particles were not completely covered by MgSnY particles, but MgSnY particles protected

most of the surface of Al_8Fe_4Y particles. Thus, particle A was analyzed to be a core-shell particle that has Al_8Fe_4Y as a core and MgSnY as the shell.

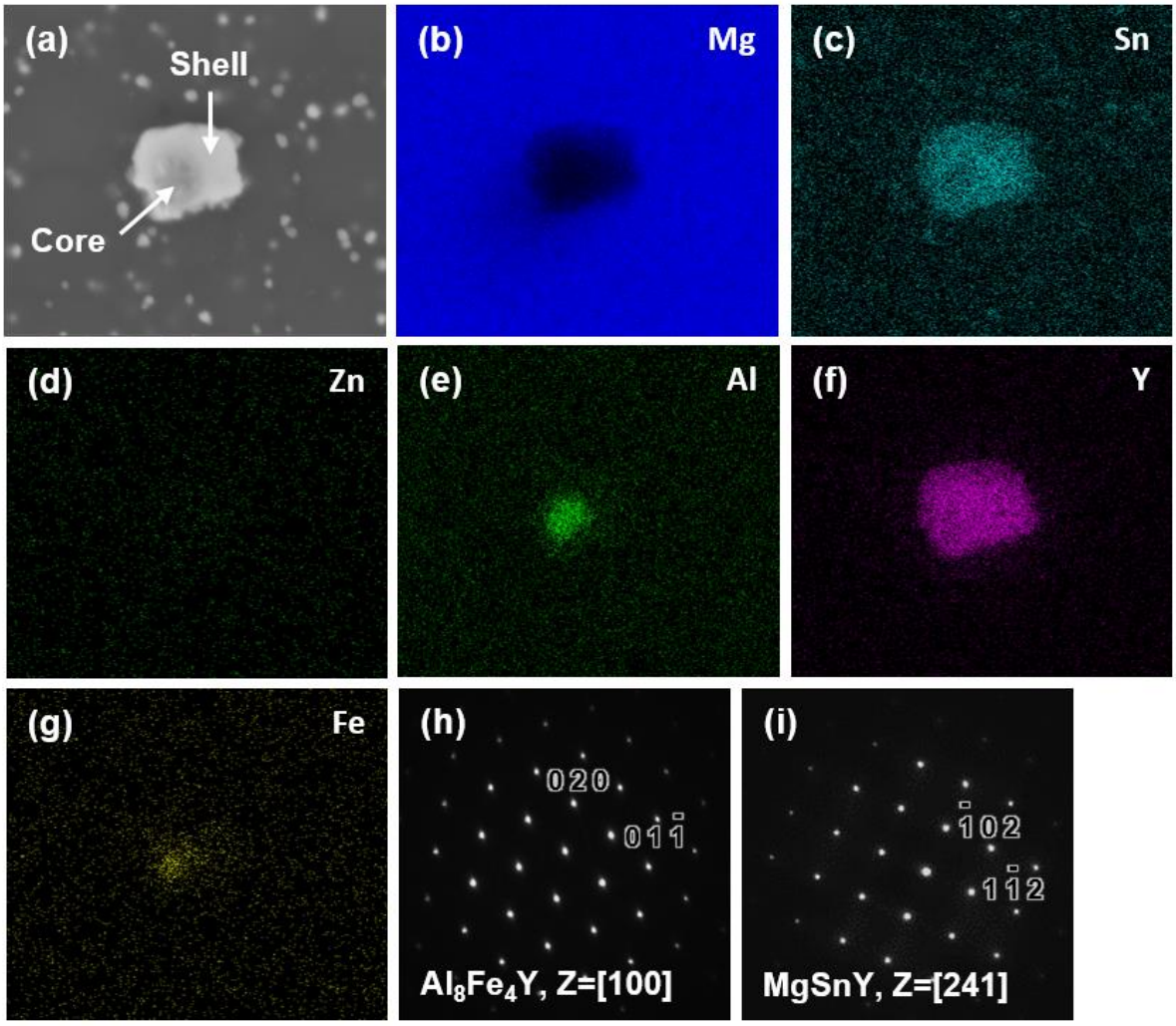

Fig. 10. (a) SEM micrograph of particle A in Fig. 9, corresponding EDS mapping images of (b) Mg, (c) Sn, (d) Zn, (e) Al, (f) Y and (g) Fe, and electron diffraction patterns of (h) core Al_8Fe_4Y and (i) shell MgSnY.

3.2.2. SKPFM measurement

SKPFM was used to measure whether the nobility of the particles has changed because of the change of intermetallic particle due to Y microalloying. Fig. 11 is a Volta potential map obtained by SKPFM, which shows the electrochemical potential difference between the Mg matrix and the particles. Compared to the Mg matrix, the Volta potential of Al_5Fe_2 particle (TZA811) was 950 mV higher, the

core of TZAW8110 was 800 mV higher, and the shell of TZAW8110 was 500 mV higher. Through Y microalloying, the Al_5Fe_2 turned into Al_8Fe_4Y and the Volta potential dropped by 150 mV. In addition, the Volta potential of the shell was measured to be 300 mV lower compared to the core.

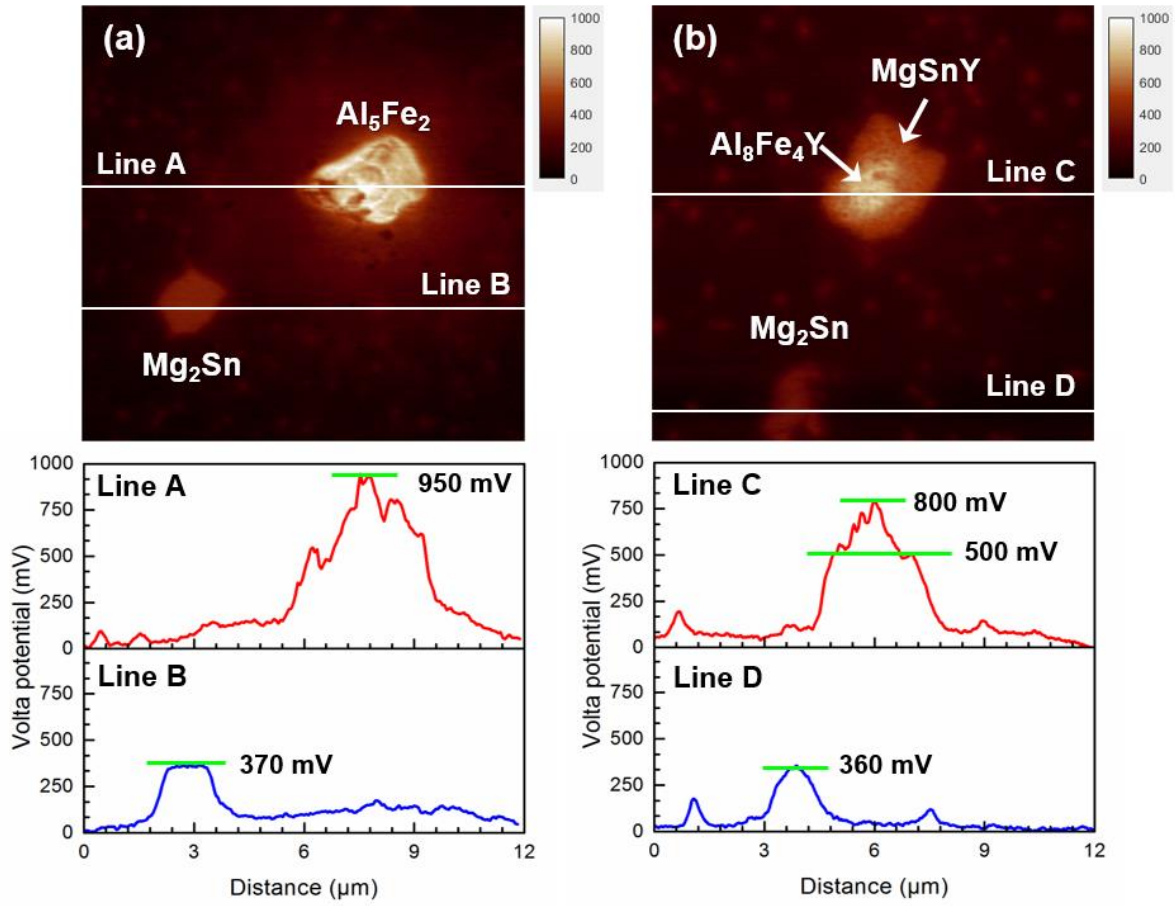

Fig. 11. SKPFM images and Volta potential profiles along the lines of the (a) TZA811 and (b) TZAW8110 alloys.

3.2.3. Corrosion development

Fig. 12 shows the corrosion development of TZA811 and TZAW8110 observed through 72 hour-span under the condition of 25 °C, 0.6 M NaCl solution. Two alloys showed the similar pattern regarding corrosion development. In both alloys, filiform corrosion was carried out after the pit initiation and pitting occurred 5 min after immersion. Through macroscopic observation, it seems that the corrosion rate is almost same up to about 24 h. However, after 72 h, there were a lot of oxide on the surface of TZA811, which was not the case of TZAW8110. This means that TZA811 has a higher corrosion rate

than TZAW8110.

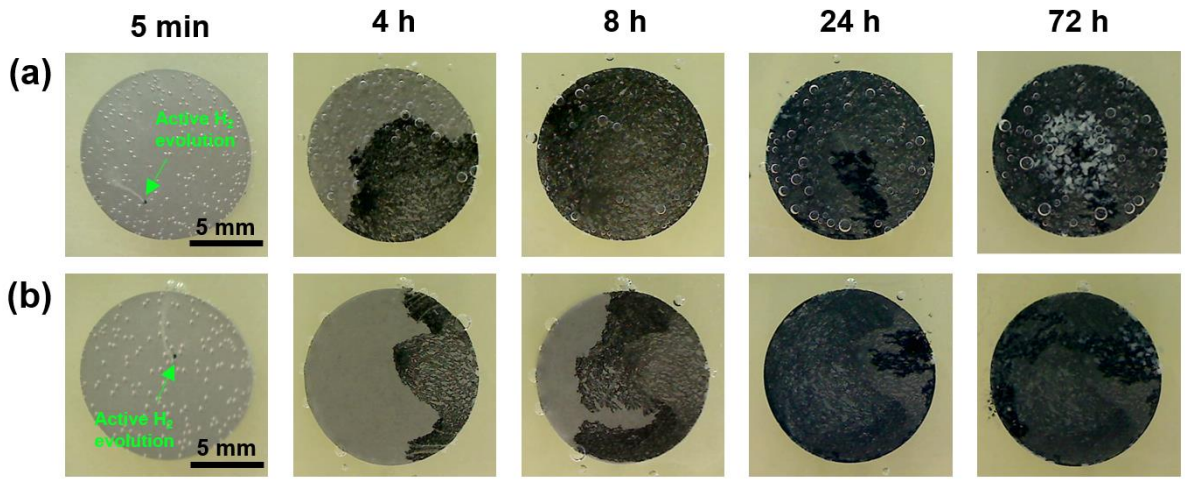

Fig. 12. Optical micrographs showing the macroscopic surfaces of the (a) TZA811 and (b) TZAW8110 alloys after immersion in 0.6 M NaCl solution for different time scale.

In order to determine if there was a difference in corrosion until 24 h, both TZA811 and TZAW8110 alloys went through immersion for 24 h and then the corrosion depths were compared. If you see Fig. 13, it shows that TZAW8110 only corroded to a depth of about 10 μm, but TZA811 corroded to a depth of almost 100 μm. This means that even if it looks similar to the eye, there is a significant difference in corrosion depth. Regarding these results, it can be said that the corrosion rate of TZA811 is higher than TZAW8110.

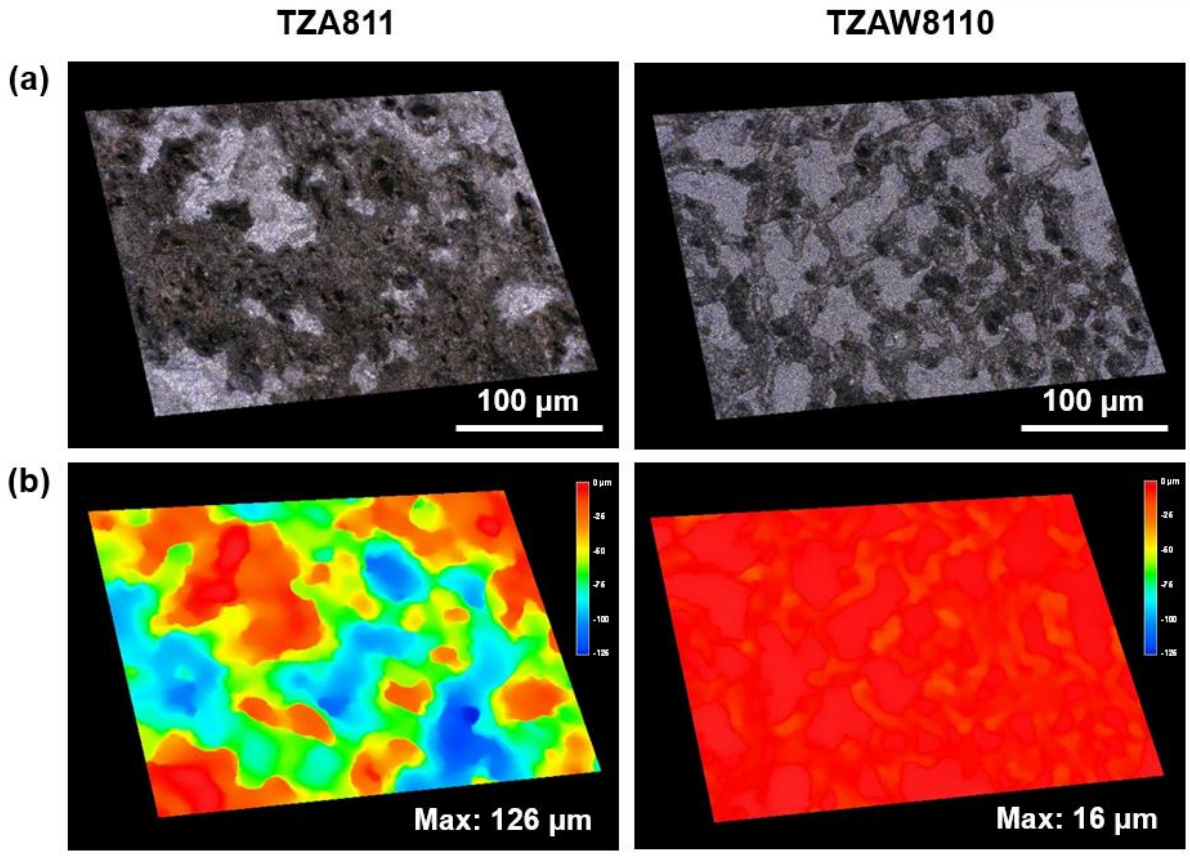

Fig. 13. (a) Optical micrographs showing the macroscopic surfaces and (b) corresponding depth profiles of the TZA811 and TZAW8110 alloys.

To see if the difference of corrosion resistance is related to the different microstructure of TZA811 and TZAW8110, SEM was used to observe the microscopic change during immersion of the two alloys. The observation was focused around the Al_5Fe_2 and core-shell particle, which is the most significant difference between the two alloys. As seen in Fig. 14, after 5 min of immersion, nearly identical amount of oxide was stacked upon the surface of Al_5Fe_2 and core-shell particle. However, after 4 h, when observing the same location of TZA811, more oxide was stacked on the Al_5Fe_2 particle and the oxide layer was destroyed. In contrast, the core-shell particle of TZAW8110 showed almost no difference. Al_5Fe_2 was constantly showing corrosion reaction in 0.6 M NaCl solution, but core-shell particle did not.

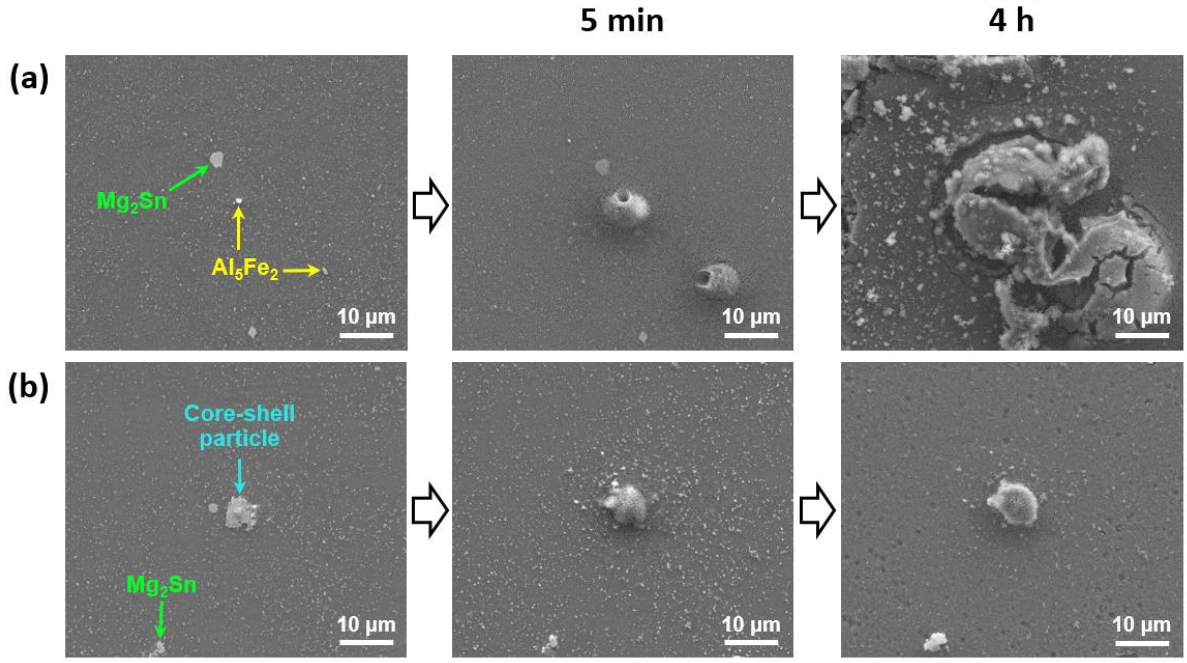

Fig. 14. SEM micrographs showing the surfaces of the (a) TZA811 and (b) TZAW8110 alloys before and after immersion in 0.6 M NaCl solution for 5 min and 4 h.

Fig. 15 (a) shows collected H_2 volume values of the TZA811 and TZAW8110 alloys for 72 h. In this figure, you can see that as the immersion time of TZA811 increases, the corrosion resistance decreases. In Fig. 15 (a), the amount of H_2 generated of TZA811 to 6 h is 0.46 ± 0.01 ml cm^{-2}, while only 0.28 ± 0.01 ml cm^{-2} of H_2 was generated in TZAW8110. However, that gap gets even bigger after 24 h. As TZA811 shows the value of 3.01 ± 0.38 while TZAW8110 generated only 1.24 ± 0.15 ml cm^{-2}. If you look at Fig. 15 (b), the amount of collected H_2 volume of the TZA811 and TZAW8110 is 9.42 ± 1.30 and 3.20 ± 0.23 ml cm^{-2}, respectively, and the mass loss is measured as 19.52 ± 2.70 mg cm^{-2} and 6.54 ± 0.70 mg cm^{-2}. The corresponding corrosion rate values of the TZA811 and TZAW8110, evaluated by the mass loss values, are 12.71 ± 1.76 and 4.24 ± 0.47 mmpy, respectively. This shows that the corrosion resistance of the TZA811 alloy increased by almost 3 times by applying Y microalloying.

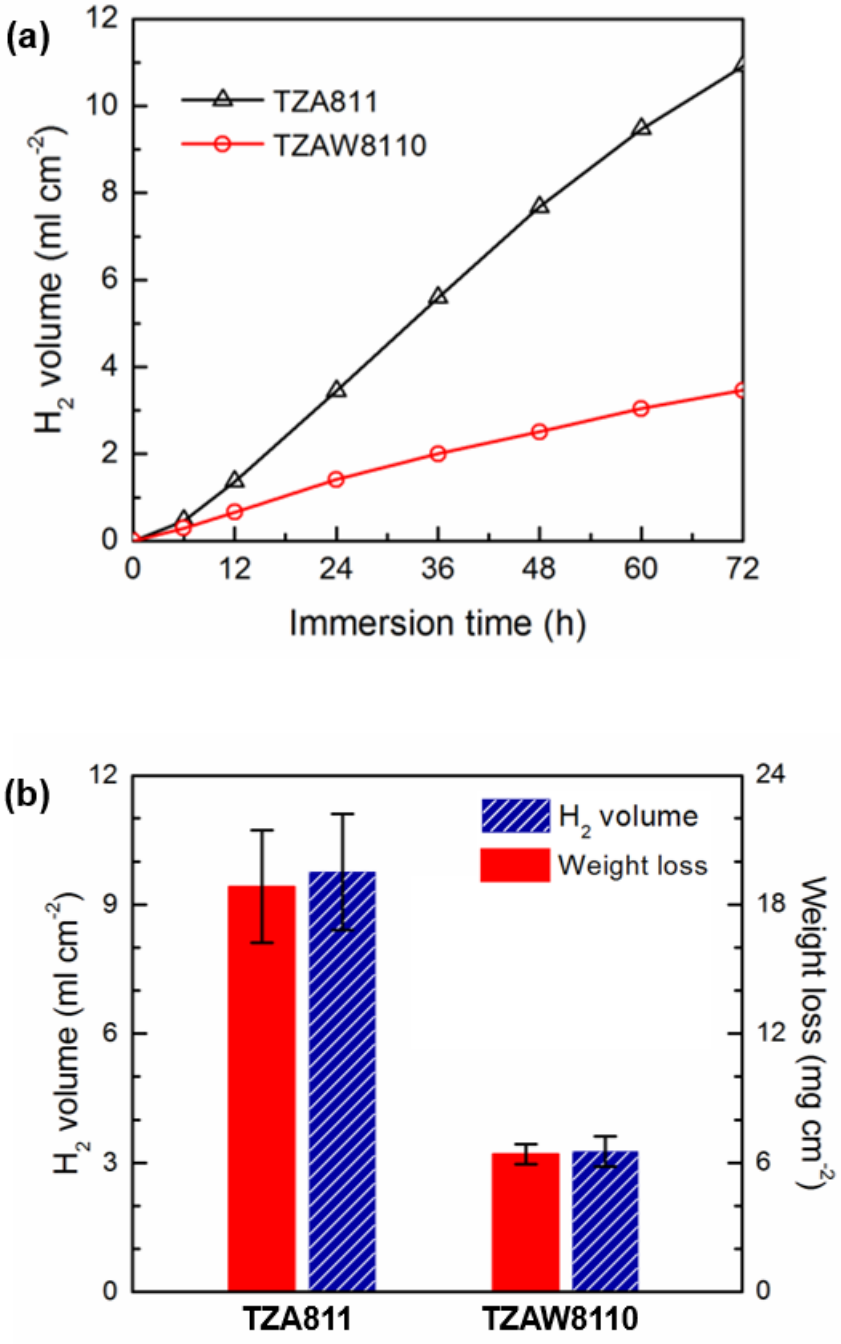

Fig. 15. (a) Collected H_2 volume values and (b) H_2 volume and mass loss values of the TZA811 and TZAW8110 alloys after immersion for 72 h in 0.6 M NaCl solution at 25 °C.

3.2.4. Potentiodynamic polarization test

Fig. 16 is the potentiodynamic polarization curves obtained in the 0.6 M NaCl solution. The E_{corr} was

approximately the same in both TZA811 and TZAW8110, showing the value of -1.61 $V_{SCE.}$ But the $i_{cathodic}$ values measured at -1.70 V_{SCE} were 0.58 ± 0.05 (TZA811), and 0.30 ± 0.06 (TZAW8110) mA cm^{-2}, showing that the $i_{cathodic}$ of TZAW8110 was smaller than that of TZA811.

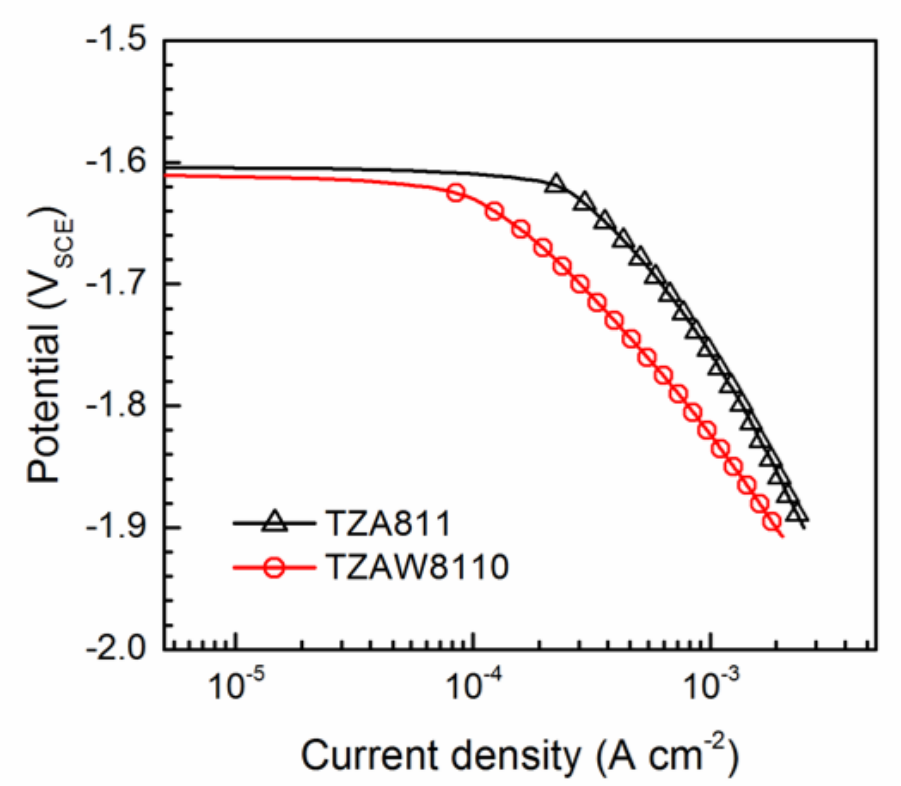

Fig. 16. Cathodic branch of the potentiodynamic polarization curves of the TZA811 and TZAW8110 alloys in 0.6 M NaCl solution.

3.3 Discussion

This study found that by 0.04wt.% Y microalloying, the corrosion resistance can be increased about 3 times. It is previously known that if Y is alloyed to Mg, Y is solutionized to the α-Mg matrix, ending up in creating a stable oxide layer, or creates a new particle that replaces the existing highly noble particle. However, in case of this alloy, the pit initiation takes place almost simultaneously in the 0.6 M NaCl solution, resulting in TZAW8110 not showing the passive behavior. In addition, the amount of Y present within the α-Mg matrix when the temperature is ranged between 25 ~ 250 °C is 6.17×10^{-21} ~ 2.57×10^{-11} wt.%, which means that Y does not affect the passivity of TZAW8110. The Y that has not been solutionized to α-Mg matrix exists in the form of an intermetallic particle such as Al_8Fe_4Y or MgSnY. The main change due to Y microalloying is replacement of Fe containing particle to a core-shell structured particle. The Al_5Fe_2 particle of TZA811, as previously reported, is known as an intermetallic particle that acts as a strong cathodic site due to its highly noble property [13]. However, due to Y microalloying, Al_5Fe_2 is changed to Al_8Fe_4Y, which has a lower Volta potential, and the Al_8Fe_4Y is covered by MgSnY, which has an even lower Volta potential than Al_8Fe_4Y. The core is composed of Al_8Fe_4Y, which still has a high Volta potential of 800 mV. However, most Al_8Fe_4Y cannot participate in the corrosion reaction since the core is protected by MgSnY, which has a low Volta potential of approximately 500 mV. The core is only participating in the corrosion reaction if it is not fully protected with MgSnY or if it is exposed due to polishing. In Fig. 14, you can see the cathodic reaction decrease due to the replacement of existing Al_5Fe_2 particles to core-shell particles. The potentiodynamic polarization test also supports this phenomenon. In the polarization curve, the $i_{cathodic}$ shows a higher value when the cathodic site consumes more electrons. In other words, as the more cathodic reaction occurs, the value of $i_{cathodic}$ becomes higher. Fig. 16 shows that because the $i_{cathodic}$ of TZAW8110 is lower than TZA811, Y microalloying reduces the cathodic reaction of TZAW8110.

IV. Influence of surface modification

4.1 Experimental

4.1.1. Specimen preparation

Table 3 shows the analyzed composition (wt.%) of the Mg–8Sn–1Zn–1Al–0.1Mn (TZAM8110) alloy used in this research. The billet used for extrusion went through induction melting using graphite crucible in a CO_2 and SF_6 atmosphere, and then the molten metal was poured into a steel mold that was preheated at 200 °C for casting. The cast billet, made with a diameter of 80 mm and a height of 150 mm, was water-quenched after being homogenized for 3 h at 500 °C. Indirect extrusion was used as the extrusion method and the preheated billet (250 °C) was extruded with a ram speed of 1.3 mm s^{-1} and an extrusion ratio of 25.

Table 3. Analyzed composition (wt.%) of the TZAM8110 alloy used in this study.

Alloy	Sn	Zn	Al	Mn	Fe	Si	Mg
TZAM8110	7.81	0.93	0.83	0.009	0.002	0.002	bal.

To see if the absence of Mg_2Sn precipitates on the surface has any significant effect on corrosion behavior and mechanical properties, some specimens went through PEB treatment. The device used for PEB treatment in this research consists of cathode, anode, solenoid, vacuum chamber, and X, Y moving stage, as shown in the schematic illustration of Fig. 17. The diameter of the electron-beam is 60 mm, and the energy density follows the three-dimensional Gaussian distribution. The length and height of the specimens did not exceed 40 mm and the PEB treatment was applied to the center of the specimen. PEB treatment was performed at a condition of 0.05 Pa Ar atmosphere, 25 keV of accelerating voltage, 7 J cm^{-2} energy density, and 5 pulse times.

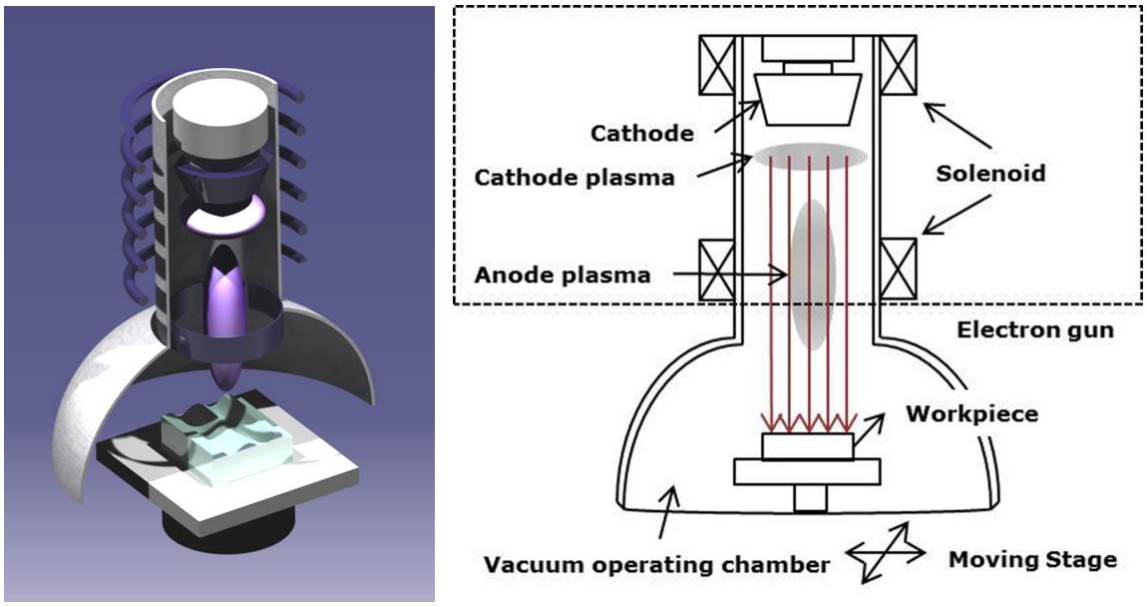

Fig. 17. Schematic illustration of the PEB treatment device.

4.1.2. Microstructure characterization

The middle part of the extruded alloy was used for observing microstructures. The observation was made on the perpendicular and parallel directions to the ED. Samples were prepared by grinding with SiC papers up to 1200 grit under a water atmosphere, and they were then polished using a 1 μm diamond paste and a 0.04 μm colloidal silica solution under an ethanol atmosphere. The microstructure was observed by using OM and the Quanta 200 SEM equipped with EDS. The grazing incidence diffraction (GID) from the Rigaku D8 Advance and Cu Kα radiation was used for X-ray diffraction (XRD) analysis.

4.1.3. Immersion and electrochemical tests

An immersion test and potentiodynamic polarization test were conducted in 25 °C, 0.6 M NaCl solution to determine the corrosion characteristics. The specimens for the immersion test was prepared in the size of 1.1 x 1.1 x 1.1 cm^3. The immersion test was conducted for 72 h. After immersion, 200 g L^{-1} CrO_3 solution was used to remove oxide; then the weight reduction was measured. Also, the amount of H_2 generated during the immersion test was measured.

For the potentiodynamic polarization test, the three-electrode cell composed of a working electrode, a SCE, and Pt plate counter electrode was used. The potentiostat was used for test. The NaCl solution

used in the test was deaerated by injecting N_2 gas. The polarization test was measured from -0.3 V_{SCE} versus E_{corr} to E_{pit}, based on the scan rate 1 mV s^{-1}. All potentiodynamic polarization tests were repeated three times each.

4.1.4. Tensile test

The tensile test was conducted under the initial strain rate of 1×10^{-3} s^{-1} and the temperature of 25 °C, using a flat tensile specimen that has a gage length / width / thickness of 32 mm / 5 mm / 1.4 mm. Prior to the tensile test, all the tensile specimens were polished in the water atmosphere using a SiC paper up to 1200 grit. In the case of the PEB-treated specimens, they went through an electron beam treatment (25 keV, 5 pulses) on both sides of the flat specimens. In case of the T4-treated specimens, they went through the heat treatment for 10 min on a furnace that was preheated at 500 °C; the specimens were then water-quenched. The experiment was repeated twice for each condition.

4.2 Results

4.2.1. Microstructure

Fig. 18 shows the SEM micrographs of the as-extruded, PEB-treated, and T4-treated specimens of TZAM8110 alloy. Fig. 18 (a) is the SEM micrographs for the as-extruded specimens. The white particle is the Mg_2Sn precipitate generated during the extrusion process. Also, you can see that Mg_2Sn precipitates with the size of tens ~ hundreds nm are evenly distributed across the as-extruded specimens. Fig. 18 (b) shows specimens that went through PEB treatment (25 keV, 5 pulses) on the vertical section to the ED. If you look at the surface and cross-section micrograph of the PEB-treated specimen, you can see that the Mg_2Sn precipitates have been removed only to the depth of 10 μm from the surface and the morphology of the area deeper than 10 μm is identical to that of the as-extruded specimen. Fig. 18 (c) shows the T4-treated specimens; you can see that the T4-treated specimen is precipitate free since it was heated at 500 °C for 10 min.

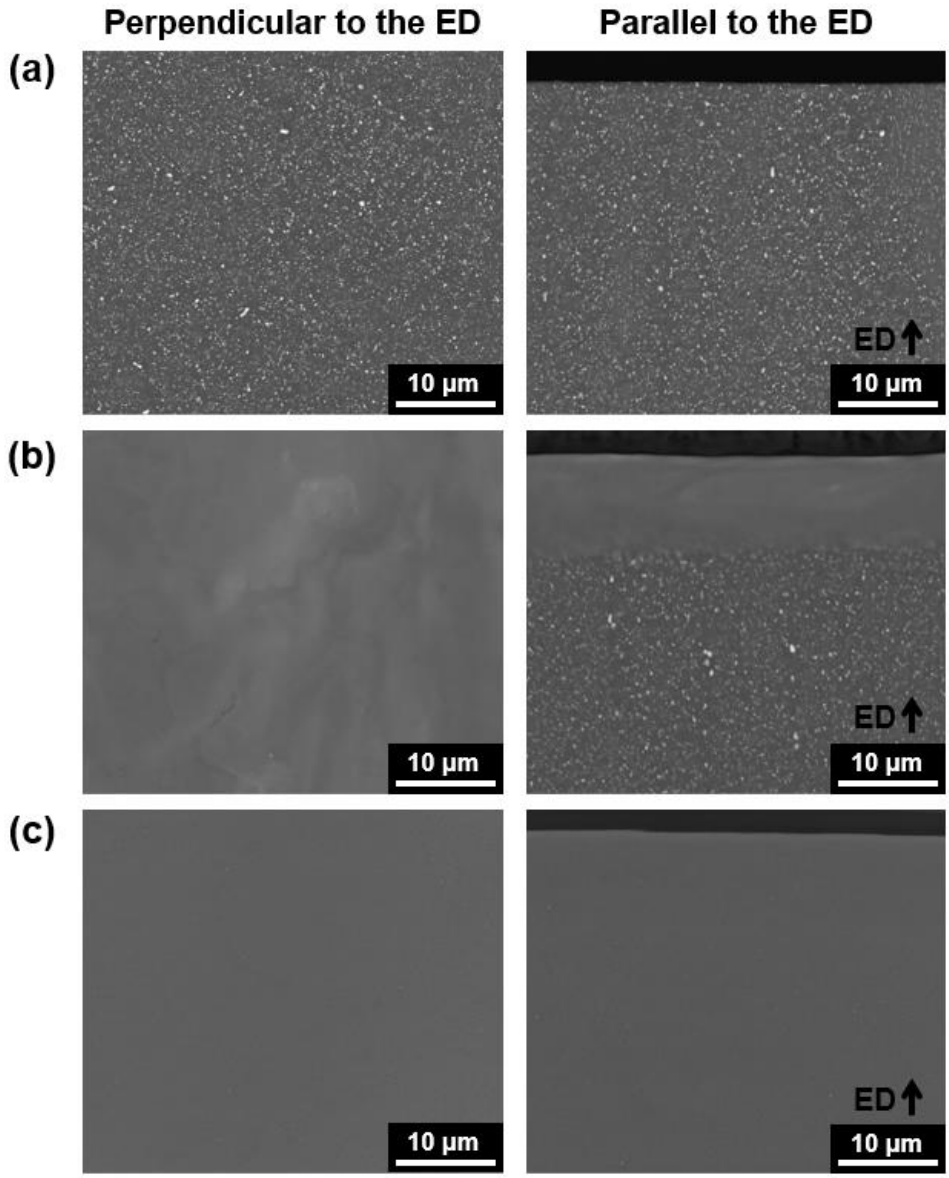

Fig. 18. SEM micrographs of the (a) as-extruded, (b) PEB-treated, and (c) T4-treated specimens.

XRD was used to see if the Mg_2Sn precipitates were removed due to PEB treatment. Fig. 19 is the results of the XRD analysis on the as-extruded specimen and PEB-treated specimen. It is seen that a diffraction peak of α–Mg and Mg_2Sn appears on the as-extruded specimen. However, in the PEB-treated specimen, you can observe that the Mg_2Sn diffraction peak has disappeared and the Mg_2Sn of the non-precipitate layer has all been dissolved into the α-Mg matrix.

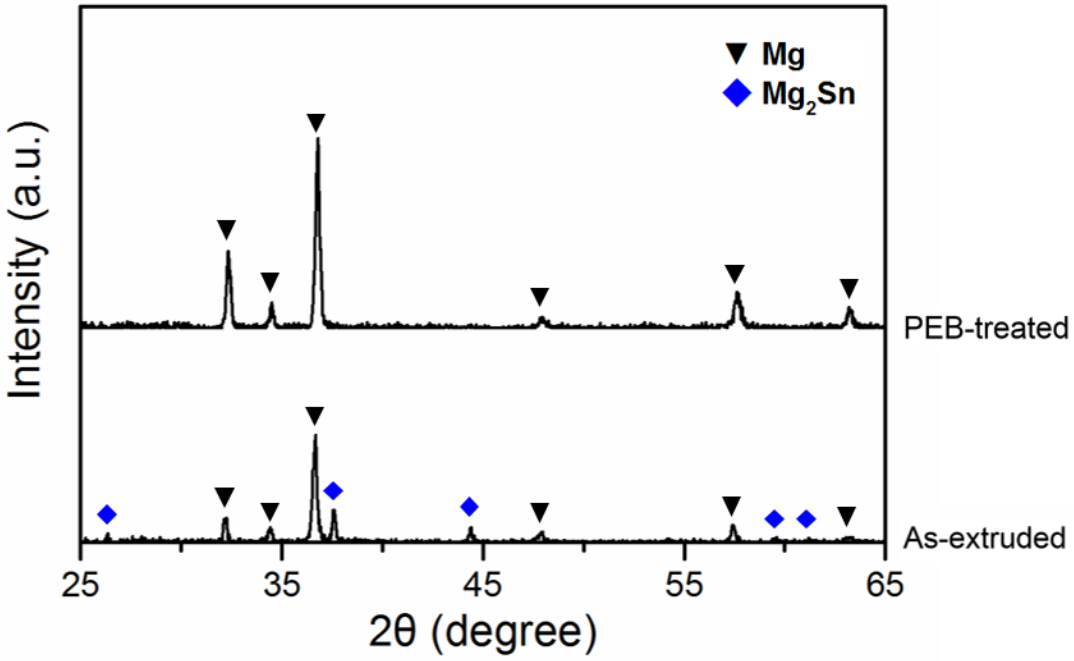

Fig. 19. XRD analysis results of the as-extruded and PEB-treated specimens.

4.2.2. Corrosion development

It was observed that the corrosion development in 25 °C, 0.6 M NaCl solution differs depending on the presence of Mg_2Sn precipitates on the surface. Fig. 20 shows 12 h long observation of the macroscopic corrosion development of as-extruded, PEB-treated, and T4-treated specimens. The as-extruded specimen, which had precipitates distributed on the surface, started to show pitting corrosion at about 10 min after immersion. On the other hand, PEB-treated and T4-treated specimens, where the precipitates on the surface were removed, generally did not show any signs of localized corrosion even after 1 h since immersion. The filiform corrosion patterns for each specimen were also very different. In the case of as-extruded specimen, the pitting started at one spot, H_2 is generated actively and filiform corrosion occurs quickly. The T4-treated specimen also shows fitting at one spot and filiform corrosion starts from that time, but the progress of corrosion is slower compared to the as-extruded specimen. In the case of PEB-treated specimen, the filiform corrosion started at various locations, but the progress of corrosion was slow, like T4-treated specimen.

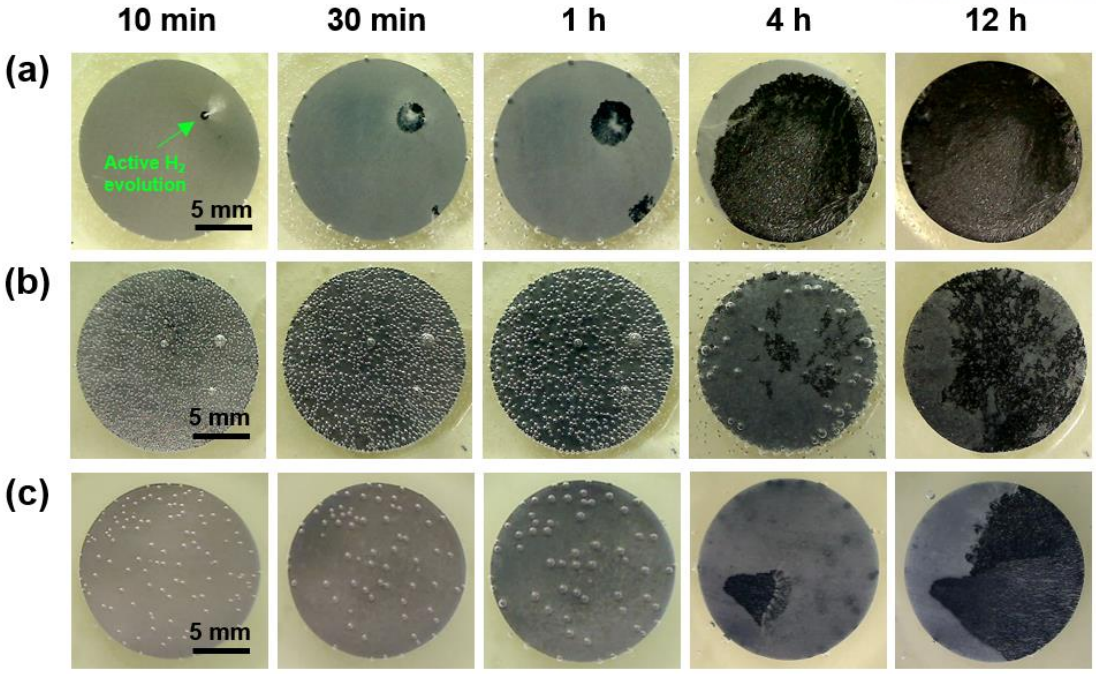

Fig. 20. Optical micrographs showing the macroscopic surfaces of the (a) as-extruded, (b) PEB-treated, and (c) T4-treated specimens after immersion in 0.6 M NaCl solution.

In Fig. 21, the depths of corrosion between the as-extruded specimen and PEB-treated specimen, after 12 h of immersion are compared. The result showed that PEB-treated specimen had a better corrosion resistance, since the as-extruded specimen was corroded to the depth of 80 μm, while the PEB-treated specimen only corroded to the depth of 15 μm. After the specific time had passed being immersed in the 0.6 M NaCl solution, the corroded cross-section of the as-extruded specimen and PEB-treated specimen were observed for this comparison.

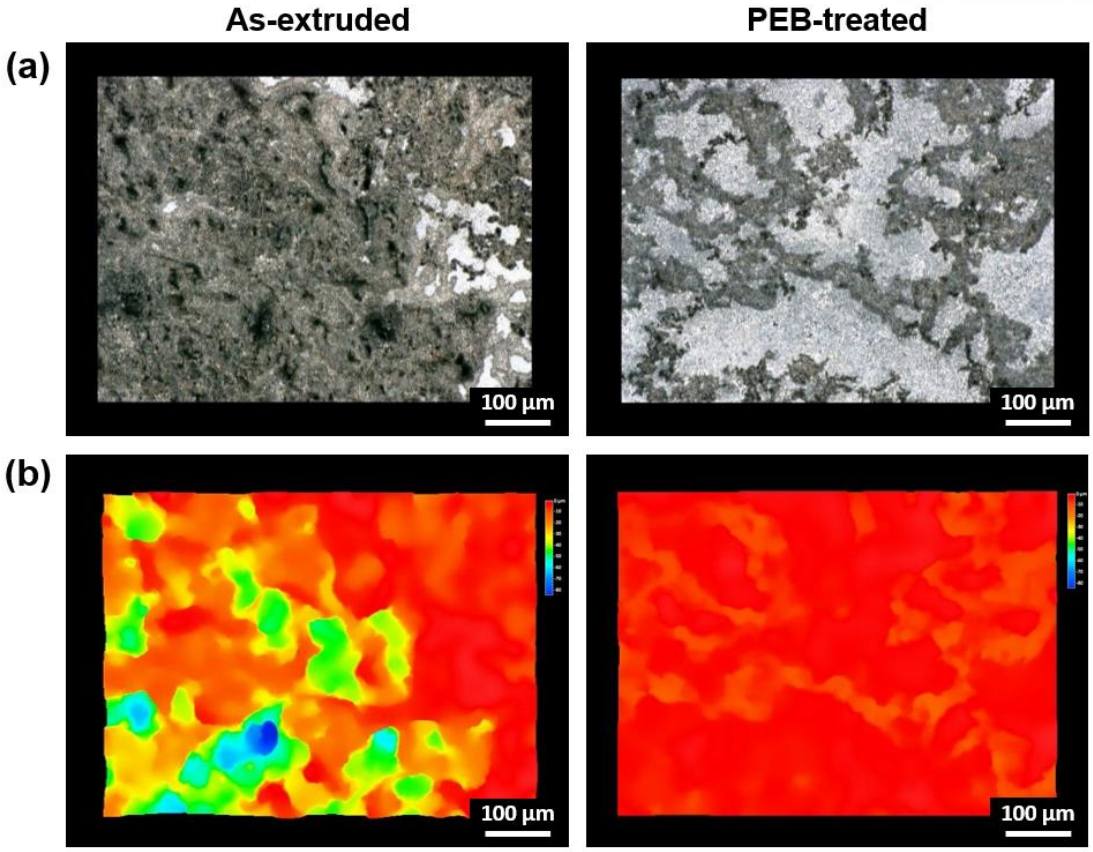

Fig. 21. (a) Optical micrographs showing the macroscopic surfaces and (b) corresponding depth profiles of the as-extruded and PEB-treated specimens.

Fig. 22 shows the state of the specimens after 30 min of immersion. In the as-extruded specimen, small pits were formed around the Mg_2Sn precipitates, but the PEB-treated specimen showed a very shallow and uniform corrosion.

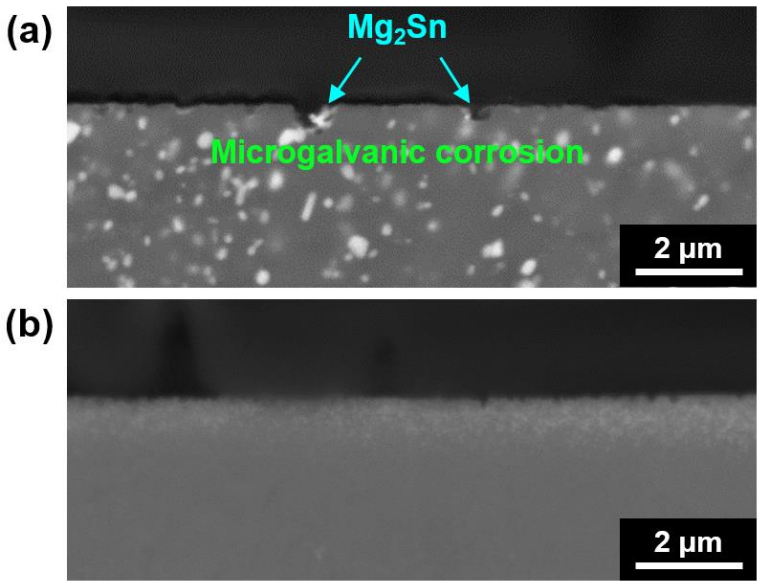

Fig. 22. Cross-sectional SEM micrographs of the (a) as-extruded and (b) PEB-treated specimens after immersion in 0.6 M NaCl solution for 30 min.

Fig. 23 shows the cross-sectional SEM micrographs of the specimens after 1 h / 4 h of immersion. As you can see, in case of the as-extruded specimen, it shows oxide and has been corroded to the depth of 10 μm, but the PEB-treated specimen shows almost no sign of corrosion on the surface. After 4 h of immersion, the as-extruded specimen is covered with oxide, meaning that the corroded area has been expanded. However, the PEB-treated specimen is only corroded partially, and the corrosion depth is so shallow that you can only observe corrosion development in the non-precipitate layer.

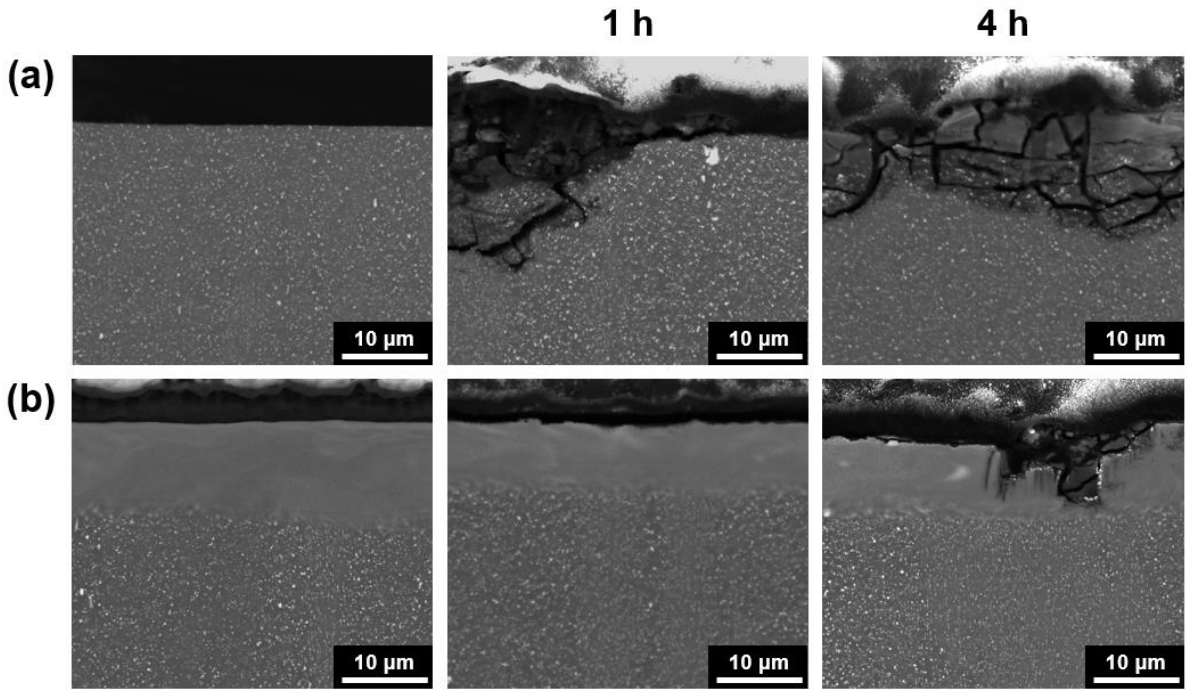

Fig. 23. Cross-sectional SEM micrographs of the (a) as-extruded and (b) PEB-treated specimens before and after immersion in 0.6 M NaCl solution for 1 h and 4 h.

4.2.3. Potentiodynamic polarization test

As presented in Fig. 24, a potentiodynamic polarization test was utilized to identify the effect of removing Mg_2Sn precipitates on the corrosion resistance. After the OCP time of 1,000 s, the polarization test was conducted. First, the E_{corr} of the PEB-treated specimen is -1.65 ± 0.02 V_{SCE} and the E_{corr} of the as-extruded specimen is -1.60 ± 0.01 V_{SCE}, which shows that the PEB-treated specimen has a lower E_{corr} compared to the as-extruded specimen. The PEB-treated specimen also had a lower $i_{cathodic}$ compared to the as-extruded specimen. At -1.80 V_{SCE}, the $i_{cathodic}$ of each as-extruded and PEB-treated specimen was -0.54 ± 0.09, -0.15 ± 0.06 mA cm^{-2}, respectively.

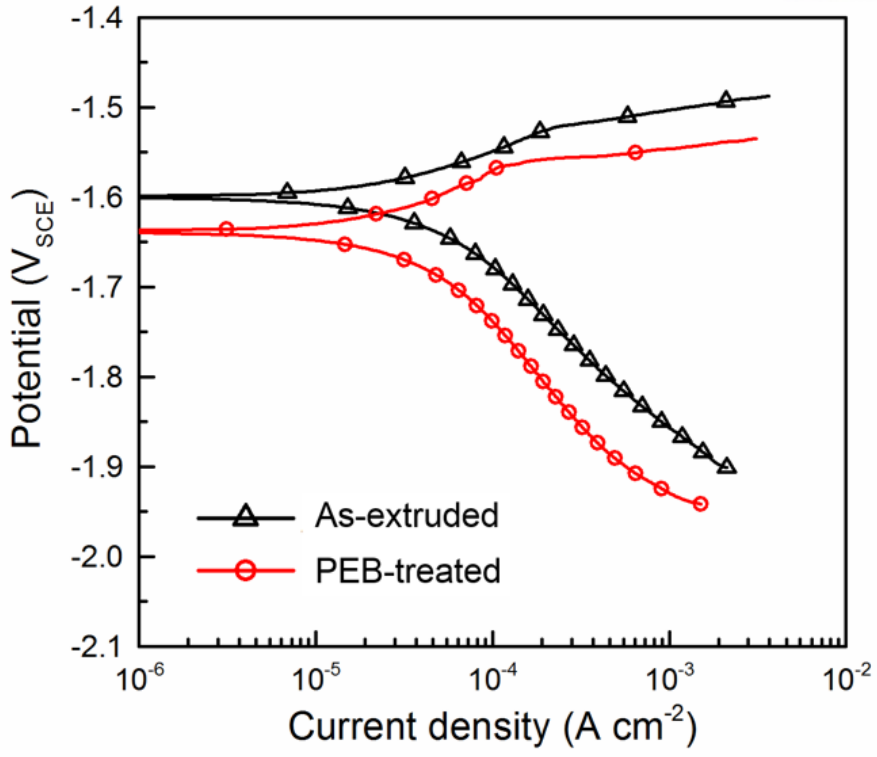

Fig. 24. Potentiodynamic polarization curves of the as-extruded and PEB-treated specimens in 0.6 M NaCl solution.

4.2.4. Corrosion evaluation

By measuring the H_2 evolution volume and mass loss values of as-extruded, PEB-treated, and T4-treated specimens at 25 °C, 0.6 M NaCl solution, we could identify how much the corrosion resistance had been improved by PEB treatment. As seen in Fig. 25, after the immersion for 72 h, the collected H_2 volume values were 5.33, 3.03, and 2.67 ml cm^{-2} and the mass loss values were 11.71, 6.87, and 6.24 mg cm^{-2} for the as-extruded, PEB-treated, and T4-treated specimens, respectively. The corresponding corrosion rates, calculated by the mass loss values, were 7.79, 4.56 and 4.15 mmpy, for the as-extruded, PEB-treated, and T4-treated specimens, respectively.

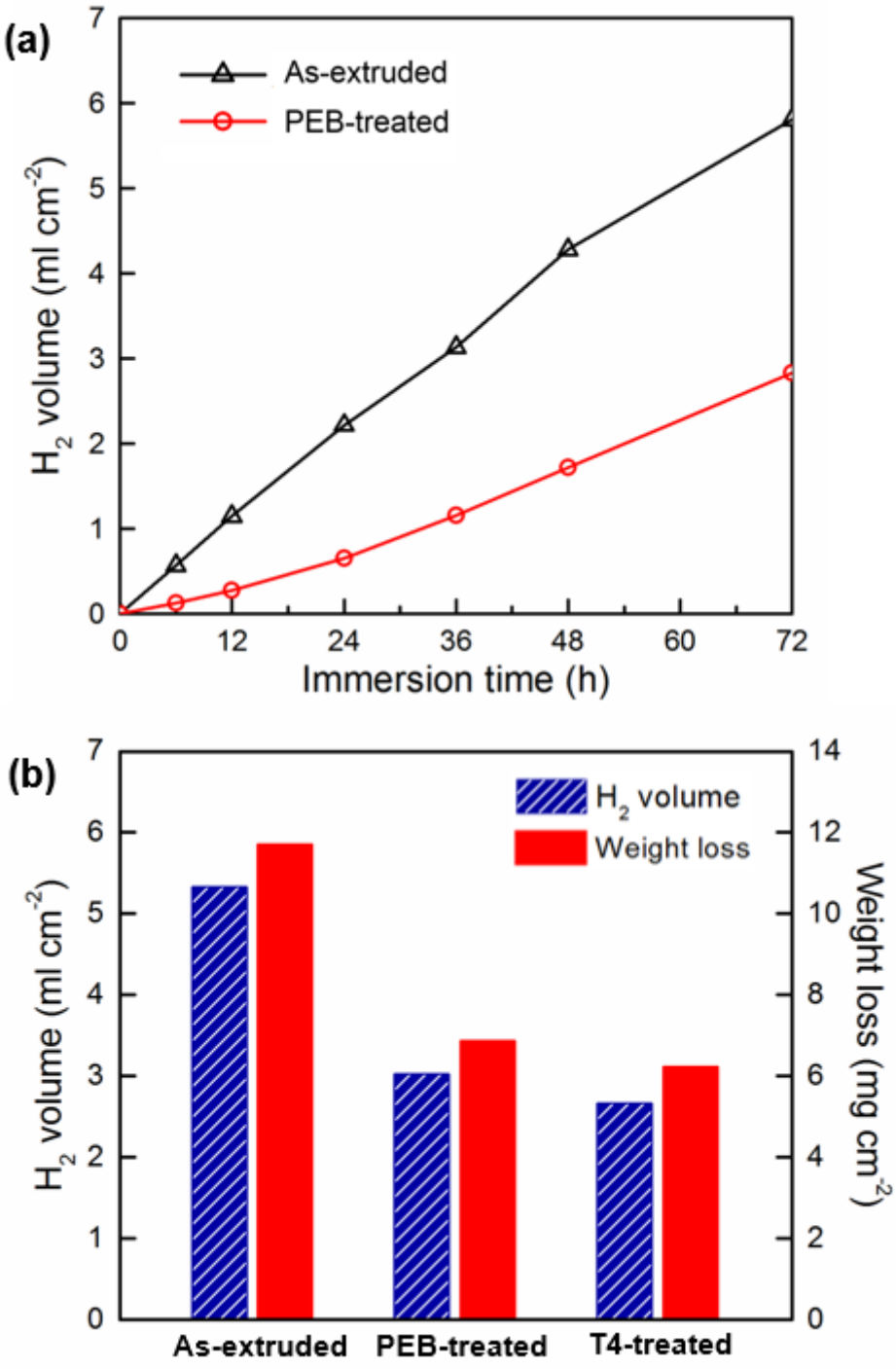

Fig. 25. (a) Collected H_2 volume values of the as-extruded and PEB-treated specimens and (b) average H_2 volume and mass loss values of the as-extruded, PEB-treated, and T4-treated specimens after immersion for 72 h in 0.6 M NaCl solution at 25 °C.

4.2.5. Evaluation of tensile properties

Mg_2Sn precipitates are closely related to mechanical properties as well as to the corrosion resistance. Tensile strength was measured to see if the mechanical strength was reduced due to the PEB treatment. Fig. 26 shows the tensile stress-strain curves of the as-extruded, PEB-treated, and T4-treated specimens at room temperature. The as-extruded specimens had the highest yield and ultimate strength of 258.5 ± 13.4 and 329.9 ± 0.1 MPa and the T4-treated specimens seemed to have the lowest yield and ultimate strength with 155.1 ± 4.8 and 228.3 ± 0.4 MPa, which is almost 100 MPa lower compared to the as-extruded specimens. The PEB-treated specimens showed the yield and ultimate strength of 237.1 ± 1.7 and 321.2 ± 0.1 MPa.

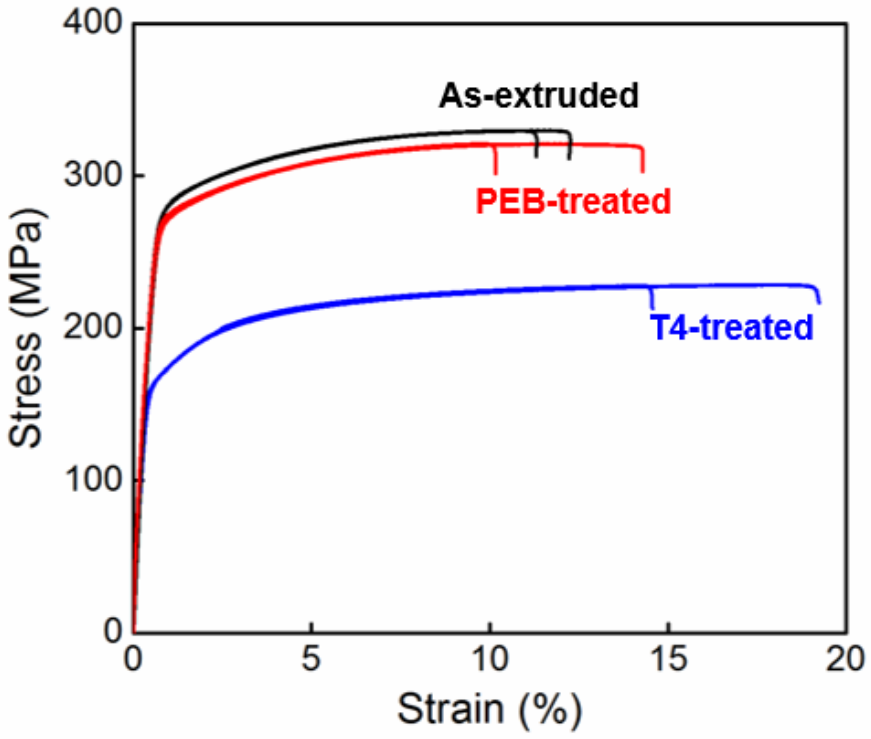

Fig. 26. Engineering stress–strain curves of the as-extruded, PEB-treated, and T4-treated specimens.

4.3 Discussion

By observing Fig. 22, it can be said that if Mg_2Sn precipitates exist, the α-Mg matrix and Mg_2Sn precipitates form a galvanic cell and influence the corrosion resistance. Although the nobility of the Mg_2Sn precipitates is not very high, it still has enough difference in electrochemical potential with the Mg matrix to form a galvanic cell. As seen in Fig. 22, Mg_2Sn precipitates acted as a cathodic site, corroding the matrix adjacent to the Mg_2Sn precipitates. But in the case of the PEB-treated specimen, which has no precipitates on the surface, it showed a relatively uniform corrosion. In Fig. 25 (a), the H_2 evolution rate of the PEB-treated specimen slightly increases. This appears to be a phenomenon due to the expanded filiform corrosion, which leads to the increased exposure of the precipitates deep inside the specimen, ultimately resulting in higher corrosion rate. In Fig. 24, you can see that the $i_{cathodic}$ of PEB-treated specimen is lower than that of the as-extruded specimen, and this can prove that the PEB treatment has reduced the cathodic reaction.

However, in contrast to $i_{cathodic}$, if you compare the i_{anodic} values of the potentiodynamic polarization curve, you can see that the i_{anodic} of PEB-treated specimen is higher than that of the as-extruded specimen, and this means that there will be a more active reaction to produce oxide at PEB-treated specimen. This is because Sn, which was used as the alloying element for Mg alloying, increases the anodic activity of alloy [47]. Due to PEB treatment, Mg_2Sn dissolves into the α-Mg matrix, leading to higher Sn content, increasing i_{anodic}. But, since Mg alloys do not have a stable oxide layer and are easily destroyed, the anodic curve is not suitable to explain the long-term corrosion reaction. Also, it is shown that both the as-extruded specimen and the PEB-treated specimen do not have a passive region on the anodic curve. Therefore, inhibiting galvanic corrosion by removing the precipitates is undoubtedly the main reason for increasing the corrosion resistance of TZAM8110.

V. Conclusion

Two methods were used to improve the corrosion resistance of the Mg–Sn–Al-based alloys. The first one was Y microalloying, and the second one was to remove the Mg_2Sn on the surface by using PEB treatment.

By the first method, the average corrosion rate of the TZA811 (Mg–8Sn–1Zn–1Al) alloy was significantly reduced from 12.71 to 4.24 mmpy by microalloying with 0.04wt.% Y. This is because Y had changed the highly noble Al_5Fe_2 particle within the TZA811 alloy to a core-shell particle with Al_8Fe_4Y and MgSnY, which led to a decrease in nobility and cathodic activity.

By the second method, I found the possibility of further improving the corrosion resistance of the Mg–Sn-based alloy by applying a PEB treatment on TZAM8110 (Mg–8Sn–1Zn–1Al–0.1Mn) alloy, which is a type of Mg–Sn-based alloy that has high corrosion resistance. As a result, by selectively removing the Mg_2Sn precipitates on the surface, it was able to successfully have a better corrosion resistance while maintaining high tensile strength. The yield strength was similar to the as-extruded specimen, but the average corrosion rates of as-extruded, PEB-treated, and T4-treated specimens were 7.79, 4.56, and 4.15 mmpy, respectively. Since the Mg_2Sn precipitates on the surface disappeared, the cathodic activity had decreased, leading to a better corrosion resistance. Also, the Mg_2Sn precipitates were removed to only a depth of 10 μm after the PEB treatment, so the PEB-treated specimen revealed a similar level of tensile strength as compared to the as-extruded specimen.

VI. References

[1] Wenwen, D., Yangshan, S., Xuegang, M., Feng, X., Min, Z., & Dengyun, W. (2003). Microstructure and mechanical properties of Mg–Al based alloy with calcium and rare earth additions. *Materials Science and Engineering: A*, *356*(1-2), 1-7.

[2] Kang, D. H., Park, S. S., & Kim, N. J. (2005). Development of creep resistant die cast Mg–Sn–Al–Si alloy. *Materials Science and Engineering: A*, *413*, 555-560.

[3] Kang, D. H., Park, S. S., Oh, Y. S., & Kim, N. J. (2007). Effect of nano-particles on the creep resistance of Mg–Sn based alloys. *Materials Science and Engineering: A*, *449*, 318-321.

[4] Wei, S., Chen, Y., Tang, Y., Liu, H., Xiao, S., Niu, Zhao, Y. (2008). Compressive creep behavior of as-cast and aging-treated Mg–5 wt% Sn alloys. *Materials Science and Engineering: A*, *492*(1-2), 20-23.

[5] Kim, B. H., Lee, S. W., Park, Y. H., & Park, I. M. (2010). The microstructure, tensile properties, and creep behavior of AZ91, AS52 and TAS652 alloy. *Journal of Alloys and Compounds*, *493*(1-2), 502-506.

[6] Gibson, M. A., Fang, X. Y., Bettles, C. J., & Hutchinson, C. R. (2010). The effect of precipitate state on the creep resistance of Mg–Sn alloys. *Scripta Materialia*, *63*(8), 899-902.

[7] Park, S. H., Kim, S. H., Kim, H. S., Yoon, J., & You, B. S. (2016). High-speed indirect extrusion of Mg–Sn–Al–Zn alloy and its influence on microstructure and mechanical properties. *Journal of Alloys and Compounds*, *667*, 170-177.

[8] Sasaki, T. T., Oh-Ishi, K., Ohkubo, T., & Hono, K. (2006). Enhanced age hardening response by the addition of Zn in Mg–Sn alloys. *Scripta Materialia*, *55*(3), 251-254.

[9] Mendis, C. L., Bettles, C. J., Gibson, M. A., & Hutchinson, C. R. (2006). An enhanced age hardening response in Mg–Sn based alloys containing Zn. *Materials Science and Engineering: A*, *435*, 163-171.

[10] Sasaki, T. T., Yamamoto, K., Honma, T., Kamado, S., & Hono, K. (2008). A high-strength Mg–Sn–Zn–Al alloy extruded at low temperature. *Scripta Materialia*, *59*(10), 1111-1114.

[11] Ding, H., Liu, L., Kamado, S., Ding, W., & Kojima, Y. (2008). Study of the microstructure, texture and tensile properties of as-extruded AZ91 magnesium alloy. *Journal of alloys and compounds*, *456*(1-2), 400-406.

[12] Kim, H. J., Kim, B., Baek, S. M., Sohn, S. D., Shin, H. J., Jeong, H. Y., ... & Park, S. S. (2015). Influence of alloyed Al on the microstructure and corrosion properties of extruded Mg–8Sn–1Zn alloys.

Corrosion Science, *95*, 133-142.

[13] Ha, H. Y., Kim, H. J., Baek, S. M., Kim, B., Sohn, S. D., Shin, H. J., ... & Lee, J. G. (2015). Improved corrosion resistance of extruded Mg–8Sn–1Zn–1Al alloy by microalloying with Mn. *Scripta Materialia*, *109*, 38-43.

[14] Baek, S. M., Kang, J. S., Kim, J. C., Kim, B., Park, S. S., & Shin, H. J. (2018). Improved corrosion resistance of Mg–8Sn–1Zn–1Al alloy subjected to low-temperature indirect extrusion. *Corrosion Science*, *141*, 203-210.

[15] Suzuki, M., Sato, H., Maruyama, K., & Oikawa, H. (2001). Creep deformation behavior and dislocation substructures of Mg–Y binary alloys. *Materials Science and Engineering: A*, *319*, 751-755.

[16] Kashefi, N., & Mahmudi, R. (2012). The microstructure and impression creep behavior of cast AZ80 magnesium alloy with yttrium additions. *Materials & Design*, *39*, 200-210.

[17] Kumar, N. R., Blandin, J. J., Suery, M., & Grosjean, E. (2003). Effect of alloying elements on the ignition resistance of magnesium alloys. *Scripta Materialia*, *49*(3), 225-230.

[18] Fan, J. F., Yang, G. C., Chen, S. L., Xie, H., Wang, M., & Zhou, Y. H. (2004). Effect of rare earths (Y, Ce) additions on the ignition points of magnesium alloys. *Journal of materials science*, *39*(20), 6375-6377.

[19] Zhang, J., Niu, X., Qiu, X., Liu, K., Nan, C., Tang, D., & Meng, J. (2009). Effect of yttrium-rich misch metal on the microstructures, mechanical properties and corrosion behavior of die cast AZ91 alloy. *Journal of Alloys and Compounds*, *471*(1-2), 322-330.

[20] Jia, R., Zhang, M., Zhang, L., Zhang, W., & Guo, F. (2015). Correlative change of corrosion behavior with the microstructure of AZ91 Mg alloy modified with Y additions. *Journal of Alloys and Compounds*, *634*, 263-271.

[21] Baek, S. M., Kang, J. S., Shin, H. J., Yim, C. D., You, B. S., Ha, H. Y., & Park, S. S. (2017). Role of alloyed Y in improving the corrosion resistance of extruded Mg–Al–Ca-based alloy. *Corrosion Science*, *118*, 227-232.

[22] Mingo, B., Arrabal, R., Mohedano, M., Mendis, C. L., del Olmo, R., Matykina, E., ... & Pardo, A. (2017). Corrosion of Mg-9Al alloy with minor alloying elements (Mn, Nd, Ca, Y and Sn). *Materials & Design*, *130*, 48-58.

[23] Ha, H. Y., Kang, J. Y., Kim, S. G., Kim, B., Park, S. S., Yim, C. D., & You, B. S. (2014). Influences of metallurgical factors on the corrosion behaviour of extruded binary Mg–Sn alloys. *Corrosion Science*,

82, 369-379.

[24] Cheng, W. L., Park, S. S., You, B. S., & Koo, B. H. (2010). Microstructure and mechanical properties of binary Mg–Sn alloys subjected to indirect extrusion. *Materials Science and Engineering: A*, *527*(18-19), 4650-4653.

[25] Wu, J., Allain-Bonasso, N., Zhang, X. D., Zou, J. X., Hao, S. Z., Grosdider, T., & Dong, C. (2010). Low energy high current pulsed electron beam treatment for improving surface microstructure and properties. In *IOP Conference Series: Materials Science and Engineering* (Vol. 12, No. 1, p. 012010). IOP Publishing.

[26] Hao, S., Gao, B., Wu, A., Zou, J., Qin, Y., Dong, C., ... & Guan, Q. (2005). Surface modification of steels and magnesium alloy by high current pulsed electron beam. *Nuclear Instruments and Methods in Physics Research Section B: Beam Interactions with Materials and Atoms*, *240*(3), 646-652.

[27] Gao, B., Hao, S., Zou, J., Wu, W., Tu, G., & Dong, C. (2007). Effect of high current pulsed electron beam treatment on surface microstructure and wear and corrosion resistance of an AZ91HP magnesium alloy. *Surface and Coatings Technology*, *201*(14), 6297-6303.

[28] Li, M. C., Hao, S. Z., Wen, H., & Huang, R. F. (2014). Surface composite nanostructures of AZ91 magnesium alloy induced by high current pulsed electron beam treatment. *Applied Surface Science*, *303*, 350-353.

[29] Hao, S., & Li, M. (2016). Producing nano-grained and Al-enriched surface microstructure on AZ91 magnesium alloy by high current pulsed electron beam treatment. *Nuclear Instruments and Methods in Physics Research Section B: Beam Interactions with Materials and Atoms*, *375*, 1-4.

[30] Song, G. L. (Ed.). (2013). *Corrosion prevention of magnesium alloys*. Elsevier.

[31] J. D. Hanawalt, C. E. Nelson, and J. A. Peloubet. (1942). Corrosion Studies of Magnesium and Its Alloys. *Trans. Am. Soc. Mining Metall. Eng., 147,* 273-99

[32] J. E. Hillis and R. W. Murray. (1987). Finishing alternatives for high purity Mg alloys. In *SDCE 14th International Die Casting Congress and Exposition, G-T, 87-003*

[33] Olsen, A. L. (1991). Corrosion characteristics of new magnesium alloys. *Translation of Paper presented at the Bauteil*, *91*, 1-21.

[34] Frey, D., & Albright, L. L. (1984, June). Development of a Mg alloy structural truck component. In *Proceedings of the 41st world Mg conference, London*.

[35] Song, G., & Atrens, A. (2003). Understanding magnesium corrosion—a framework for improved alloy performance. *Advanced engineering materials*, *5*(12), 837-858.

[36] Cole, G. S. (2003). Issues that influence magnesium's use in the automotive industry. In *Materials Science Forum* (Vol. 419, pp. 43-50). Trans Tech Publications.

[37] Yang, L., Zhou, X., Liang, S. M., Schmid-Fetzer, R., Fan, Z., Scamans, G., ... & Thompson, G. (2015). Effect of traces of silicon on the formation of Fe-rich particles in pure magnesium and the corrosion susceptibility of magnesium. *Journal of Alloys and Compounds*, *619*, 396-400.

[38] Lunder, O., Nisancioglu, K., & Hansen, R. S. (1993). *Corrosion of die cast magnesium-aluminum alloys* (No. 930755). SAE Technical Paper.

[39] Song, G., Atrens, A., Wu, X., & Zhang, B. (1998). Corrosion behaviour of AZ21, AZ501 and AZ91 in sodium chloride. *Corrosion science*, *40*(10), 1769-1791.

[40] Srinivasan, A., Ningshen, S., Mudali, U. K., Pillai, U. T. S., & Pai, B. C. (2007). Influence of Si and Sb additions on the corrosion behavior of AZ91 magnesium alloy. *Intermetallics*, *15*(12), 1511-1517.

[41] Cao, F., Shi, Z., Hofstetter, J., Uggowitzer, P. J., Song, G., Liu, M., & Atrens, A. (2013). Corrosion of ultra-high-purity Mg in 3.5% NaCl solution saturated with Mg (OH) 2. *Corrosion science*, *75*, 78-99.

[42] Cao, F., Shi, Z., Song, G. L., Liu, M., & Atrens, A. (2013). Corrosion behaviour in salt spray and in 3.5% NaCl solution saturated with Mg (OH) 2 of as-cast and solution heat-treated binary Mg–X alloys: X= Mn, Sn, Ca, Zn, Al, Zr, Si, Sr. *Corrosion Science*, *76*, 60-97.

[43] Kim, K. H., Nam, N. D., Kim, J. G., Shin, K. S., & Jung, H. C. (2011). Effect of calcium addition on the corrosion behavior of Mg–5Al alloy. *Intermetallics*, *19*(12), 1831-1838.

[44] Standard, A. S. T. M. G1, 2003, Standard Practice for Preparing, Cleaning, and Evaluating Corrosion Test Specimens, ASTM International, West Conshohocken, PA, 2003, DOI: 10.1520/G0001-03.

[45] Song, G., Atrens, A., & StJohn, D. (2001). An hydrogen evolution method for the estimation of the corrosion rate of magnesium alloys. *Magnesium Technology 2001*, 254-262.

[46] Jones, D. A. (1996). Principles and Prevention of Corrosion, 2nd. *Ed. Upper Saddle River, NY: Prentice Hall*, 168-198.

[47] Gusieva, K., Davies, C. H. J., Scully, J. R., & Birbilis, N. (2015). Corrosion of magnesium alloys: the role of alloying. *International Materials Reviews*, *60*(3), 169-194.